SCANNING PROBE MICROSCOPY FOR OPTOELECTRONIC CHARACTERIZATION AT THE NANOSCALE

A THESIS

SUBMITTED TO THE GRADUATE PROGRAM OF MATERIAL

SCIENCE AND NANOTECHNOLOGY

AND THE INSTITUTE OF ENGINEERING AND SCIENCES

OF BILKENT UNIVERSITY

IN PARTIAL FULFILLMENT OF THE REQUIREMENTS

FOR THE DEGREE OF

MASTER OF SCIENCE

By

Mustafa Ürel

August, 2010

I certify that I have read this thesis and that in my opinion it is fully adequate, in scope and in quality, as a thesis for the degree of Master of Science.

Prof. Dr. Salim Çıracı(Advisor)

I certify that I have read this thesis and that in my opinion it is fully adequate, in scope and in quality, as a thesis for the degree of Master of Science.

Asst. Prof. Aykutlu Dânâ(Co-advisor)

I certify that I have read this thesis and that in my opinion it is fully adequate, in scope and in quality, as a thesis for the degree of Master of Science.

Dr. M. Bilge İmer (Co-advisor)

Approved for the Institute of Engineering and Science:

Prof. Dr. Levent Onural
Director of the Institute Engineering and Science

ABSTRACT

SCANNING PROBE MICROSCOPY FOR OPTOELECTRONIC CHARACTERIZATION AT THE NANOSCALE

Mustafa Ürel
M.S. in Material Science and Nanotechnology
Supervisor: Prof. Dr. Salim Çıracı
August, 2010

In this work, we propose methods for electrical characterization of nanostructured surfaces using electrostatic force and tunneling current measurements in scanning probe microscopy. Resolution smaller than 10 nm in electrostatic force microscopy (EFM) is attained and reasons for this attainment is explained in terms of the tip-sample capacitance and mechanical vibrations of tip design. Dynamic measurements are done in EFM using a lumped model for tip-sample electrostatic interaction instead of a simple tip-sample capacitance model. Surface photovoltage measurements are done and assured in EFM using frequency response techniques. Also, combining tunneling current measurements by EFM measurements, optoelectonic properties of graphene/graphene oxide samples are characterized.

Keywords: Electrostatic force microscopy, Scanning Tunneling Microscopy, Graphene, Graphene oxide, Surface Photovoltage.

ÖZET

TARAMA SONDA MİKROSKOBU İLE NANOMETRE DÜZEYİNDE ELEKTRİKSEL KARAKTERİZASYON

Mustafa Ürel
Malzeme Bilimi ve Nanoteknoloji , Yüksek Lisans
Tez Yöneticisi: Prof. Dr. Salim Çıracı
Ağustos, 2010

Bu çalışmada, nano yapıda olan yüzeylerin tarama sonda mikroskobu kullanılarak, elektrostatik kuvvet ve tünelleme akımı ölçümleri yoluyla karakterizasyonu için yöntemler öneriyoruz. Bunun için, elektrostatik kuvvet mikroskobunda (EKM) 10 nm'den daha kücük düzeyde çözünürlük elde edildi ve bu neticenin elde edilebilmesinin sebepleri uç-nümune kapasitansı ve ucun tasarımından kaynaklanan mekanik titreşimler cinsinden izah edildi. EKM'de uç-nümune etkileşimleri basit bir uç-nümune kapasitansı modelinden daha genişletilmiş bir devre ile modellenerek incelendi. Yüzey fotovoltajı ölçümleri yapıldı ve bu ölçümün EKM'de doğrulanması frekans tepkisi de ölçülerek sağlandı. Ayrıca, EKM ölçümlerini, tünelleme akımı ölçümleriyle birleştirerek, grafen/grafen oksit nümunelerinin optoelektronik özellikleri karakterize edildi.

Anahtar sözcükler: Elektrostatik kuvvet mikroskobu, Tarama Tünelleme Mikroskobu, Grafen, Grafen oksit, Yüzey Fotovoltaji.

Acknowledgement

I would like to express my gratitude to my advisors Prof. Salim Çıracı and Prof. Aykutlu Dânâ for their priceless guidance. Also, I would like to thank Dr. M. Bilge İmer who was my advisor for 1.5 years of my M.S. study and did not leave me alone until taking my M.S. degree.

I thank to my groupmate Okan Öner Ekiz for his discussions and the samples that we have analyzes.

I would like to thank to my groupmates M. Kurtuluş Abak and Hasan Güner for their guidance in atomic force microscopy and clean room fabrication issues. Also, I thank to Koray Mızrak, Hüseyin Vural, Reha Özalp, Semih Yaşar, Fikret Piri and other UNAM staff for their help.

Also I would like to thank Sencer Ayas, Yavuz Nuri Ertaş for being my everlasting friends.

I am grateful to my parents' Tuncay and Filiz Ürel for their infinite patience and advice.

I would also like to thank my office mates Mehmet Kanık and Tural Khudiyev. Also, I am grateful to Abdullah Soylu, Fırat Vargün, Tolga Özaslan, Kadir Akbudak, Salih Kanlıdağ, Kürsad Durmaz for their discussions.

I gratefully acknowledge TÜBITAK for the financial support.

Contents

List of Figures

List of Tables

Chapter 1

Introduction

Since its invention, atomic force microscopy (AFM) has found wide applications in surface characterization. AFM is dubbed "the lab on a tip" and is a major research field itself. The predecessor scanning tunneling microscopy (STM) , from which atomic force microscopy was firstly derived, is also taking attention and new techniques are discovered and applied on it. Although STM has very good lateral resolution. AFM has many modes of use including contact, non-contact and intermittent contact modes and their applications to many different electrical characterization techniques allow a very wide range of spectroscopy techniques. For example, for the non-contact and intermittent contact mode, frequency modulation and amplitude modulation techniques are used. For electrical applications, scanning gate microscopy, kelvin probe microscopy, electrostatic force microscopy are just a few examples. Having these many techniques, there is an important research in this family. With the increasing need for thin film mechanical and electrical characterizations, biological and chemical researches in liquid environment, scanning probe microscopy is an important and very involved subject of research.

1.1 Problem Statement and Motivation

Tunneling microscopy methods have intrinsically high resolution that features smaller than tip radius can be seen. But characterization techniques using tunneling micrsocopy may change surface properties considerably, such that there can be either vulnerable structures or mobile domains on the tip or on the sample. Also, low conductance samples may be hard to image because of the low tunneling current levels. Therefore, understanding the surface electrical properties without passing any current is necessary. To measure electrical properties without passing an electrical current through sample, electrostatic force microscopy (EFM) is used. EFM measures the electrostatic force between the tip and the sample using a suitable DC bias to obtain enough signal contrast. But electrostatic forces are rather long range forces, the sample not only interacts with the tip apex but also with the bulk of the tip and even with the cantilever leading to considerable drop in resolution.

In this work, we have developed a tip design to improve EFM resolution to smaller than 10 nm in ambient conditions. Simultaneous high resolution measurement of first and second time harmonics of electrostatic force is made possible which made a considerable amount of information which is not available otherwise. Also, a surface photovoltage detection method together with impedance characteristics of the surface was developed using EFM. By joining EFM methods with scanning spreading resistance microscopy (SSRM), many properties that were not available by only using one method was extracted from the samples. Electrochemical changes can be done using conductive tips. We demonstrated such tip-induced modifications on graphene devices. Also, a fabrication method for preparing a sample consisting of many electronic devices to be analyzed under AFM was developed.

1.2 Organization of the Thesis

We begin in Chapter 2 by an introduction to the theory and applications of electrostatic force microscopy (EFM). The tip design, fabrication and reason for better resolution, EFM theory, simultaneous measurements of both time harmonics and also the surface photovoltage and substrate resistance and capacitance models are explained in this chapter. Next, in Chapter 3, we have explained tunneling current measurements and scanning spreading resistance microscopy (SSRM). In Chapter 4, graphene and graphene oxide samples are characterized by using the explained electrical methods in Chapters 2 and 3. Finally, in Chapter 5, method for analyzing many-electronic device samples that contain hard to analyze structures under EFM is given and potential graphene device applications by tip induced reduction and oxidation is discussed.

Chapter 2

Electrostatic force microscopy methods

2.1 High Resolution Electrostatic Force Microscopy

Electrostatic force imaging is a low resolution measuring tool in comparison to the topographic measurements for which atomic resolution can be attained. In electrical force measurements, the available resolution is far away from atomic resolution. In vacuum conditions, the resolution is much better than ambient conditions. For electrostatic force microscopy, in vacuum conditions, best resolution reported was about 10 nm. In ambient conditions, 10-15 nm resolution was recently achieved using multifrequency methods[3]. For contact potential difference measurements, using Kelvin probe microscopy, 100 nm resolution is expected in general. Electrostatic forces are characterized by long range interaction. Therefore, between the surface and the tip, not only the tip apex interacts, but also bulk of the tip and the cantilever are included in the interaction. For best resolution, the ideal case is the existence of only tip apex and sample interaction. In this context, the tip shape effects on electrical measurements resolution was previously reported[5]. The tip shape changes the tip-sample capacitance so that measurements done on the surface is an average over a large area, decreasing

the resolution. Therefore, by modifying the tip shape, the resolution could be improved. To reduce the contribution of the bulk and the cantilever, bulk volume should be decreased, and cantilever should be further away. However, doing this may result in other consequences that reduce the resolution, such as the tip vibration effects. In this section, we will present a way of increasing resolution to better than 10 nm together by eliminating unwanted mechanical vibration.

2.1.1 Tip-fabrication and the mechanical properties

The cantilever spring constants of commercial tips may range from 0.1 N/m to a few hundred N/m. Higher order flexural modes have higher effective spring constants. The given range of spring constants is also true for lateral spring constants, which are used for the measurement of dissipative forces[7, 8]. The geometry of the tips made of silicon has a pyramidal shape, which is a result of selective etching of silicon in crystallographic orientation. Because of the 45^o angle of this selective etching, bulk volume of the tip is very high. The tips we have used are non-contact mode tips, coated by a layer of 50 nm of Pt in Gatan PECS system. After Pt coating, the tip and cantilever becomes conductive, which is necessary for electrical measurements. After that, using the FEI FIB system, tips of 5 nm radius was obtained. The design of the tip is shown in Figure 2.1. The left-hand side shows the model of the design, and the right-hand side shows the image taken in SEM.

Tip design

A small radius conductive tip has a sharper tip apex, and also the interaction of the tip body with the sample is decreased since the volume is decreased. Also the cantilever is made further away from the sample. But if there is a single very thin rod, as the tip scanning the surface, the lateral force coming from the topographical features makes the tip vibrate laterally with a higher amplitude and longer period, since a long and a thin rod has a smaller spring constant. This causes instabilities in imaging. To prevent this, a long rod of acceptable spring

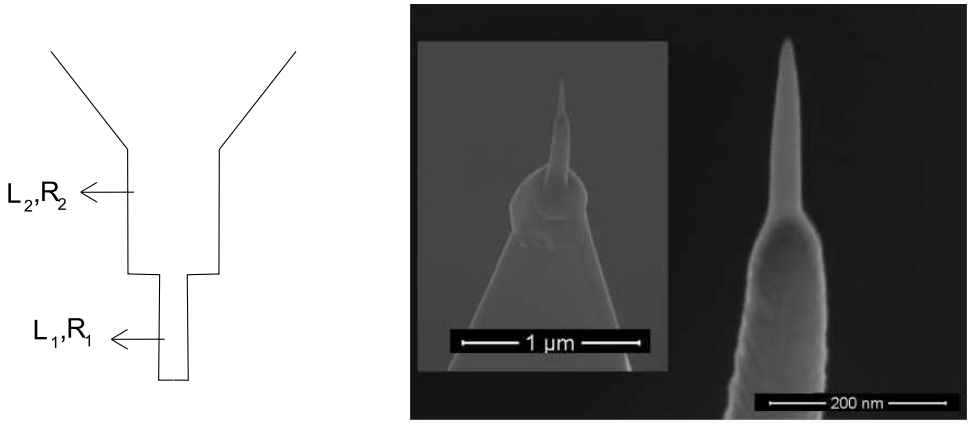

Figure 2.1: Pt-needle tip design. Needle consists of two rods of different diameters. The bottom rod has larger radius, but it is still very thin (L_2, R_2) and the radius of the end rod is ultra thin (L_1, R_1) that is related with the high resolution. Bottom rod is much longer than the end rod.

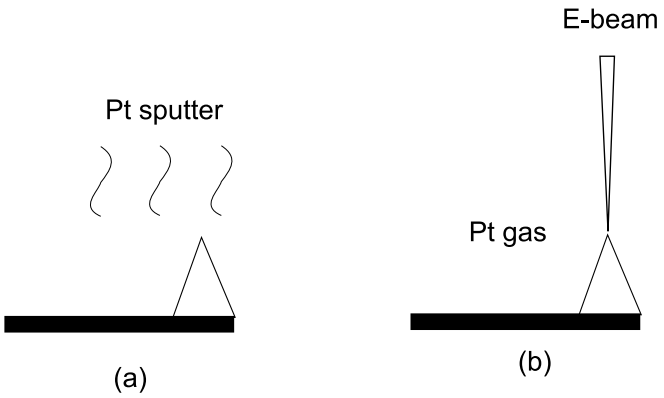

Figure 2.2: The steps of two-part tip fabrication (a) If tip is not conductive this step should be done. (b) In this step, using E-beam induced deposition (EBID), two-part tip, high effective spring constant, 5 nm tip radius tip is fabricated.

constant should be built, such that with its length cantilever interactions can be minimized and with its low thickness the bulk interactions can be reduced. After that, a very thin rod of shorter length should be deposited on the long rod, keeping the effective spring constant of the two rod system acceptable and reducing the tip apex, so that electrostatic interaction is on only a small area, increasing the resolution. The rods can be thought of as serially connected springs, which vibrate in their radial directions. The spring constant of a rod in its radial direction is given as,

$$k = \frac{3\pi E}{4}\frac{R^4}{L^3} \tag{2.1}$$

where R is the radius of the rod and L is the length of the rod. The effective spring constant of the serially connected rod system is,

$$k_{eff} = \frac{k_1 k_2}{k_1 + k_2} \tag{2.2}$$

The change of effective spring constant can be viewed from Figure 2.3. To illustrate the change of spring constant, the ratios of the lengths and diameters of the rods are taken into consideration. Graph gives an intuition for designing tip to affect the spring constant better. The k_{eff} value should be much greater than both the flexural and the lateral spring constants of the cantilever. For, then bending is effectively just from the cantilever. Then the order of k_{eff} is about to be or greater than 100 N/m which is at least an order higher than the cantilever's spring constant. For higher flexural or lateral modes, since spring constant is proportional to the square of the mode frequency ($k\ \alpha\ f_{mode}$), a much higher k_{eff} is required. Having much higher k_{eff} also means that much lower amplitude, much higher frequency oscillations are generated in the tip while scanning, which does not disturb the stability, because amplitude is neglibigle and oscillations are better averaged out in each sampling and affects the feedback system less. By decreasing the length of the thin rod, and increasing the radius of the thick rod, we can achieve higher effective spring constants and lower oscillation amplitudes, which will degrade less the stability of imaging, and hence the resolution of the image.

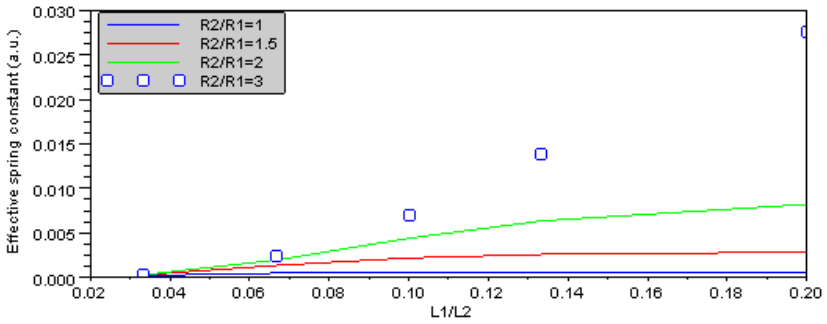

Figure 2.3: Graph of effective spring constant vs length of the thin rod part of the tip. Insets belong to different diameters of the thick section.

2.2 Tip-sample capacitance

In a standard electromagnetic course, the capacitance is defined as,

$$C = \frac{Q}{V} \tag{2.3}$$

where Q is the total stored charge, and V is the applied potential between two contacts of the capacitor. The tip-sample capacitance can be analysed using very different models. Parallel plate capacitor is a very rough approximation, but it can be used to understand the results qualitatively. In a parallel plate capacitor, neglecting the fringing field at the ends of the plates, electric field E is uniform and equal to

$$E = \frac{V}{d} \tag{2.4}$$

where d is the distance between the plates. If there is a more complex shape, E can be found from the general formula

$$\vec{E} = -\nabla V \tag{2.5}$$

$$U_e = \frac{1}{2}\int \epsilon_0 \vec{E_0^2} \cdot d^3\vec{r} = \frac{1}{2} C_0 V^2 \tag{2.6}$$

The electrostatic potential energy and force and capacitance are related through the following equation.

$$F_e = -\frac{\partial}{\partial z} U_e = -\frac{1}{2} V^2 \frac{\partial}{\partial z} C \tag{2.7}$$

Hence, we can extract capacitance derivative from the obtained data. Then we can find the capacitance by assuming the capacitance zero at a far enough distance and using integration,

$$C = \int \frac{-2\vec{F_e}}{V^2} \cdot d\vec{z} \tag{2.8}$$

The tip-sample capacitance can also be analysed using sphere-plane capacitance approximation. This is in fact a very usual and very good approximation, fitting many measured data using capacitance microscopy, electrostatic force microscopy and kelvin probe microscopy. The capacitance between a conducting sphere and a plane is given by[6]

$$C_{sp} = C_{iso} \sum_{n=2}^{\infty} \frac{sinh(\alpha)}{sinh(n\alpha)} \tag{2.9}$$

where C_{iso} is the isolated sphere's capacitance given by

$$C_{iso} = 4\pi\epsilon_0 R; \tag{2.10}$$

and α is given by

$$\alpha = ln\left[1 + \frac{d}{R} + \sqrt{\frac{d^2}{R^2} + 2\frac{d}{R}}\right] \tag{2.11}$$

The series in Equation 2.9 for $z/R \gg 1$ converges to

$$C_{sp} = 2\pi\epsilon_0 R^2/d \tag{2.12}$$

For more accurate capacitance calculation, conical tip-sphere apex or hyperboloid tip model is used for the tip shape, and plane for the sample. For the conical model the force equation is given by[1]

$$F = \pi\epsilon_0 V^2 \left[\frac{R^2(1-sin\theta)}{d[d+R(1-sin\theta)]} + k^2\left(ln\frac{L}{d+R(1-sin\theta)} - 1 + \frac{Rcos^2\theta sin\theta}{d+R(1-sin\theta)}\right)\right] \tag{2.13}$$

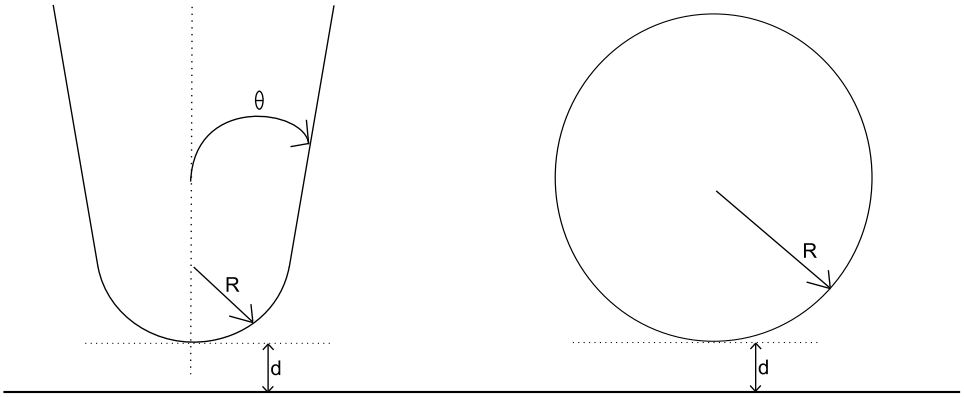

Figure 2.4: Schematic for illustration of the variables of a cone tip (left), and a sphere tip(right) model.

where $k^2 = \frac{1}{[ln(tan\theta/2)]^2}$, R is the radius of the tip apex, θ is the half aperture angle of the cone, d is the tip-sample separation distance. Figure 2.4 illustrates the models together with the defined parameters for sphere and cone models that are

Then the capacitance can be calculated by the integral in Equation 2.8.

2.2.1 EFM basics

EFM is employed on AFM, by driving the tip with a bias voltage, whose frequency is much lower than the mechanical driving frequency. However multiharmonic methods were also applied[3, 4] in which higher frequencies are used, especially at the second harmonic of the tip. Applying an electrical bias at the second flexural mode, or conversion of a low frequency component to the second or higher order flexural modes[4] are some examples. In this section, a basic theory of the electrostatic force microscopy will be given. First of all, the equations for the electrostatic force dependent on the surface-tip potential difference and the tip-surface capacitance gradient will be driven. Assuming that bias is given to the tip, we write the bias signal as

$$V_{bias} = V_{dc} + V_{ac} sin\omega t \tag{2.14}$$

where $\omega = 2\pi f$

Using Equation 2.7, we can find the total electrostatic force. Replace V by $V_{dc} + V_{ac}sin(\omega t)$, we find

$$F = -\frac{1}{2}(V_{dc} + V_{ac}sin(\omega t))^2 \frac{\partial C}{\partial z} \tag{2.15}$$

By expanding the square term, we can find out the frequency components. For $sin(\omega t)^2$, we should use $(1 - cos(2\omega t))/2$ expansion. This will generate a contribution dc term and the second harmonic term.

$$F_{dc} = -\frac{1}{2}\frac{\partial C}{\partial z}(V_{dc}^2 + \frac{V_{ac}^2}{2}) \tag{2.16}$$

$$F_{\omega} = -\frac{\partial C}{\partial z}V_{dc}V_{ac}sin(\omega t) \tag{2.17}$$

$$F_{2\omega} = \frac{1}{4}\frac{\partial C}{\partial z}V_{ac}^2 cos(2\omega t) \tag{2.18}$$

The force gradients are easily given by

$$F_{dc} = -\frac{1}{2}\frac{\partial^2 C}{\partial z^2}(V_{dc}^2 + \frac{V_{ac}^2}{2}) \tag{2.19}$$

$$F_{\omega} = -\frac{\partial^2 C}{\partial z^2}V_{dc}V_{ac}sin(\omega t) \tag{2.20}$$

$$F_{2\omega} = \frac{1}{4}\frac{\partial^2 C}{\partial z^2}V_{ac}^2 cos(2\omega t) \tag{2.21}$$

We see there are two ac signals resulting from the bias, one of them has twice frequency of other. Note that, the first harmonic is related with V_{dc}, whereas second harmonic is independent of dc bias. Also we have no knowledge of capacitance that can be obtained through the measured harmonics of electrostatic force, but the capacitance gradient.

These equations omit dynamic charging effects caused by ac bias. Nevertheless, these equations are usually enough for understanding the phenomena. For the case of charge deposition on quantum dots for instance, or exact calculation of surface electrical properties such as dielectricity and tip-surface capacitance, these omitted quantities should be taken into consideration.

Interactions between tip and sample cause the resonance frequency of oscillation to change. This can be expressed in terms of the effective spring constant concept. It is calculated in terms of free spring constant of oscillation and the force gradients just written above

$$k^{'} = k - < F'(z_0) > \tag{2.22}$$

where $F'(z_0)$ is the derivative of the electrostatic force at the equilibrium point $z = z_0$, brackets <> denote the time average and $k^{'}$ is the modified spring constant. The fundamental angular frequency in terms of spring constant is

$$\omega_0 = \sqrt{k/m} \tag{2.23}$$

Driving the tip in a high amplitude makes it affected by both attractive and repulsive regimes. This mode of operation is called intermittent contact (or tapping) mode. In the intermittent contact mode, tip may be in a region of bistabilities. When the tip is in repulsive region, the phase is lower than 90^o , whereas in attractive mode the phase is greater than 90^o. But, in the intermittent contact mode, tip is affected by both attractive and repulsive regions. Therefore, driving amplitude and set point amplitudes should be adjusted for one of them to dominate. Otherwise, tip has a bistability and height jumps or changes in contrast occurs[15].

2.3 Electrostatic force measurements using two harmonics

Extracting the first harmonic of the electrostatic force is easy compared to extracting the second harmonic. By changing the dc bias, a good contrast between different surface potential areas can be obtained. However, for the second harmonics, the only way to obtain good contrast is improving the change of dC/dz,i.e. a high second order derivative of capacitance. But, this quantity should be high only for the interaction between surface and the tip apex. As the contribution

of the bulk increases, the resolution would decrease. Figure 2.5(a), the contribution of the bulk is shown. As the half aperture angle of the cone part of the tip increases,i.e. the bulk volume increases, the first derivative of the capacitance increases, therefore the dominated contribution of the bulk conceals the gradient of tip-sample capacitance between tip apex and the sample. Therefore, the dC/dz contribution of the tip bulk and the cantilever should be minimized, and d^2C/dz^2 of the tip apex interaction should be high enough. This latter one can be easily obtained, and is not considered much, but former one should be considered.

We may define a figure of merit for understanding the improvement of the capacitance gradient.

$$FoM = \frac{\left(\frac{\partial^2 C}{\partial z^2}\right)_{cone_2} - \left(\frac{\partial^2 C}{\partial z^2}\right)_{sp}}{\left(\frac{\partial^2 C}{\partial z^2}\right)_{cone_1} - \left(\frac{\partial^2 C}{\partial z^2}\right)_{sp}} \tag{2.24}$$

where $cone_1$ and $cone_2$ denotes the two different tips modeled as a cone, and sp denotes the spherical apex. The meaning of the figure of merit is to compare the two cases of tip shapes for contributions of the bulk of the tip to the gradient of the capacitance gradient by subtracting the spherical tip apex contribution, which should be the main contribution. For a good, though not exact assumption, bulk contribution can be thought of as interference and tip apex contribution can be thought of as signal, so figure of merit compares the noise levels for the two cases.

Separation distance values around R shows the enormous contribution of the bulk of the tip in Figure 2.5(a). When $z \ll R$ or $z \gg R$, the contribution is constant. The former case is where tip is in a few atomic distances to the surface and tip apex contribution is very high but jump-to-contact may happen. The latter case is where the tip is far away from the surface, which is known as the lift mode operation, and the high resolution is lost. The figure of merit quickly decreases around $z \approx R$. This means, the signal to noise ratio will decrease. Also resolution decreases as the tip-surface distance increases. Therefore we have to be nearer to the surface in both cases. Of course, stability, jump-to-contact cases should also be considered as mentioned above. But it is good to know how much

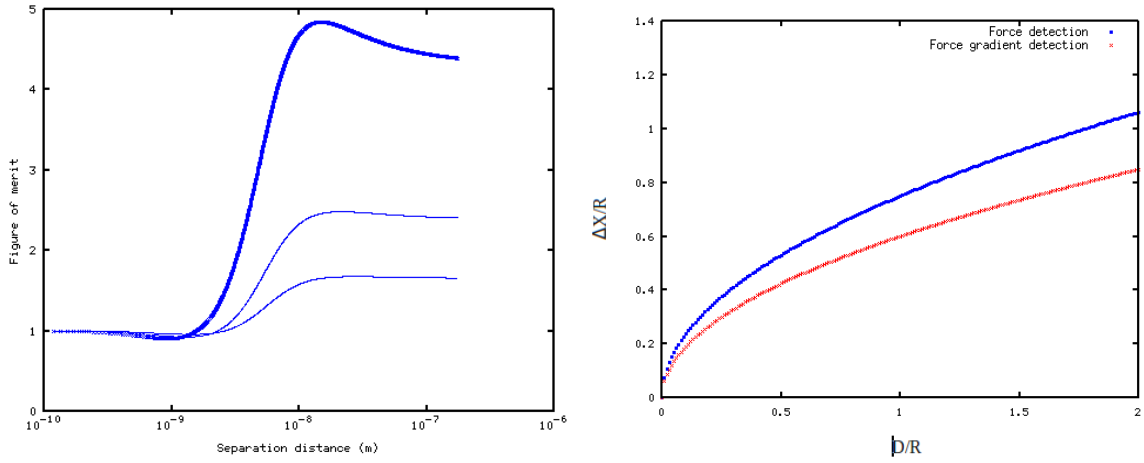

(a) (b)

Figure 2.5: Figures showing (a) the figure of merit defined in Equation 2.24 and (b) resolution (Replotted from Ref. [5]). In (a), effect of cone half aperture angle is shown. Comparison is done for $10^o, 15^o$ and 25^o to 5^o case. Aperture angle increases in the increasing figure of merit direction.

.

the separation distance affects resolution when z is on the order of R.

Tip-shape effects on electrostatic force measurement resolution can be given as a function of tip radius and separation distance. Gomez-Monivas *et al.* provide the equation $\triangle x = C\sqrt{zR}$ or , where C=0.6 for detection with force gradient, and C=0.75 for the force, $\triangle x$ is the lateral resolution, z is the separation distance and R is the tip radius[5]. Therefore, the resolution is proportional to $\sqrt{z}$. Increasing $z = R$ to $z = 2R$, we find out that figure of merit decreases about 1.3-1.5 times, and lateral resolution is lost $\sqrt{2} \approx 1.414$ times. Signal level and resolution is not lost in the same magnitude we increase the separation distance, but less than it.

2.4 Lumped model of dynamic surface potentials

2.4.1 Surface capacitance and resistance

In the electrical measurements using AFM, surface capacitance and resistance can make important contributions to the image signal. This RC circuit behaviour may cause phase shift of the current or electrostatic signal, or decrease the amplitude of the signal according to the frequency of the applied bias, that is, it has a non-negligible low-pass or high pass frequency response. Therefore, we have computed tip-sample capacitance according to our tip design. By obtaining real frequency response from the real surfaces, and assuming the simulated value of tip-sample capacitance, we have fitted the resistance and capacitance of the substrate or surface. The model circuit is shown in Figures 2.6(a) and 2.6(b)

Solving the low pass circuit is easy, so equations only for high pass will be given.

$$V_{ts} = V_{bias}\frac{1 - w^2R^2C_{ts}^2 + j\omega 2RC_{ts}}{1 - w^2R^2C_{ts}^2(1 + \frac{C}{C_{ts}}) + j\omega RC_{ts}\left(2 + \frac{C}{C_{ts}}\right)} \tag{2.25}$$

If we call the fraction term in the right hand side as $A(j\omega)$,

$$F_{ac,w}\alpha A(j\omega) \tag{2.26}$$

$$F_{ac,2w}\alpha - A(j\omega)^2 \tag{2.27}$$

and samewise for the force gradients.

There is also a phase information, which is also detectable from the electrostatic forces.

$$\angle A(j\omega) = tan^{-1}\frac{2\omega RC_{ts}}{1 - w^2R^2C_{ts}^2} - tan^{-1}\frac{(2 + \frac{C}{C_{ts}})\omega RC_{ts}}{1 - w^2R_{ts}^2C_{ts}^2(1 + \frac{C}{C_{ts}})} \tag{2.28}$$

If $A(jw)$ is obtained and tip-sample separation is exactly known by other

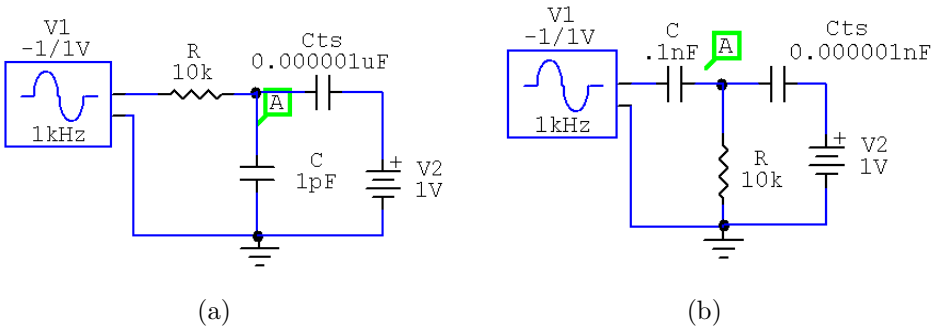

(a) (b)

Figure 2.6: (a) low pass circuit model. (b) high pass circuit model. Only the nodes that DC bias and AC bias applied are interchanged.

calibrations, then C_{ts} can be calculated from conical tip-sample capacitance model presented in Section 2.2 in Equation 2.13. Then, R and C of the surface may be fitted to the experimental data.

In Figure 2.6, two circuit models are shown. These models also show the Au/Pd control sample experiment setup, which is explained in Section 2.5. Changing only the application point of AC bias is enough to switch between low pass and high pass configurations, but an adder is needed to add AC and DC biases. But, since configuration of MFP3D Asylum setup lets the user to apply two different signals, we have used these channels. In this way, the polarity of the DC bias should be changed for obtaining the same conditions.

2.5 Surface photovoltage detection

Electrostatic force measured in EFM is dependent on the electrical properties of the tip and the sample. In the sample, the substrate may also contribute to the measured electrostatic force. Sample can be modelled by a resistor and a capacitor. If sample was a good conductor, no capacitive effect would be felt with changing frequency. But when sample is not a conductor, capacitive effects are felt. Indeed, scanning impedance microscopy or nano impedance microscopy uses this fact to take impedance map of materials. Either by measuring the tunneling current through the tip or the phase and amplitude shifts of the cantilever

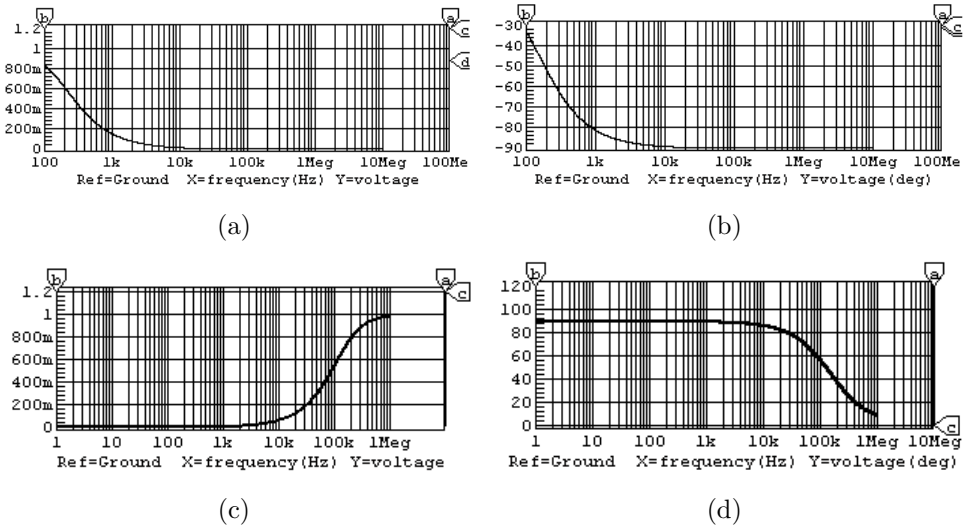

Figure 2.7: (a,c) shows the magnitude of the frequency responses of the low pass circuit (Figure 2.6(a)) and high pass circuit (Figure 2.6(b)) respectively. (b,d) Phase responses.

oscillation[9–14] across different regions, or in a frequency range for which difference of phase and amplitude can only be detected around a single frequency. But the frequency response of electrostatic forces which are detected from cantilever oscillations far away from flexural mode frequencies were not used. In this range of frequency, there are no peaks or dips other than resulting from instrumental effects, but there is a detectable change of amplitude and phase both by changing and not changing the environment, revealing the impedance characteristics of the sample. Here, we propose a method to measure surface photovoltage using electrostatic force microscopy and detection of the first time harmonics of the resulting electrostatic force to find out amplitude and phase change and hence the effect of the impedance on the measurements. Previously, surface photovoltages were detected using surface potential measurements either by Kelvin probe micrsocopy or by electrostatic force microscopy[16–19] or tunneling current microscoy[18, 20] at a range of DC bias for the latter two methods. The applied AC bias frequency is much smaller than the cantilever's fundamental oscillation frequency so that second harmonic frequency is also away from fundamental mechanical oscillation frequency of the cantilever. Amplitude and phase changes of the images can be seen both by the frequency change and the illumination intensity change. By

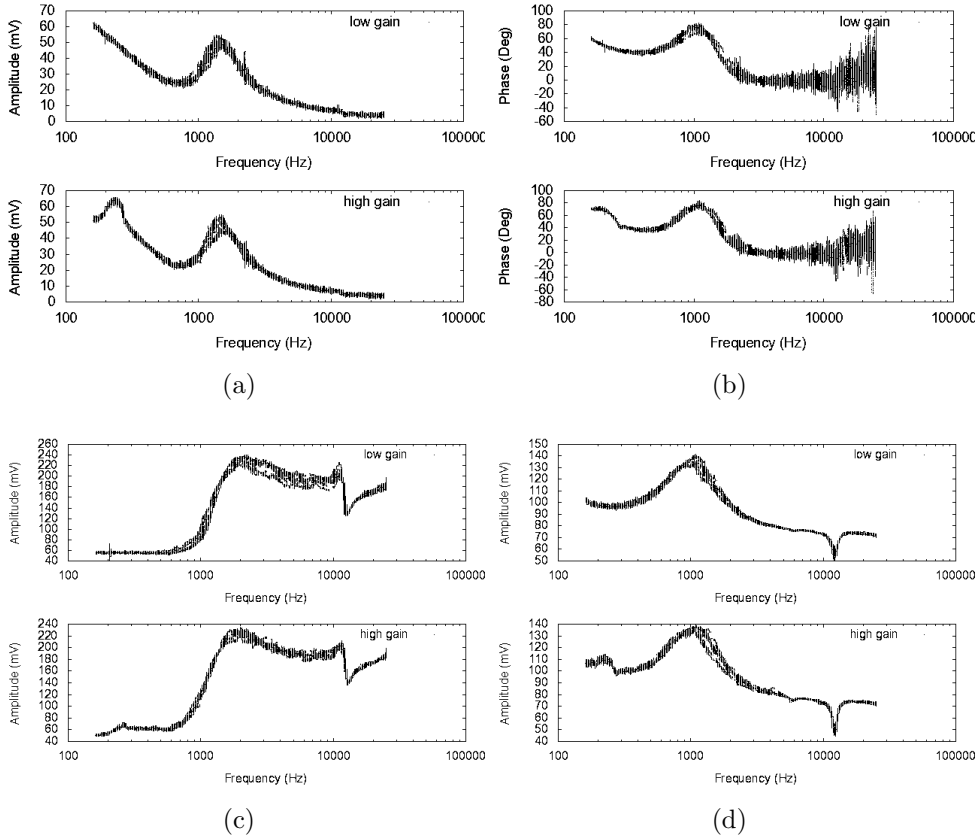

Figure 2.8: Measurements taken from Au/Pd sample. (a) and (c) shows the measured electrostatic force first harmonic amplitude for the low pass circuit and high pass circuit respectively, (b) and (d) shows the measured electrostatic force first harmonic phase for the low pass circuit and high pass circuit respectively. As seen, there are two abnormal behaviours at about 1-2 kHz and 25 kHz. The abnormal behaviour in 25 kHz is not seen in low pass amplitude measurement , and 1-2 kHz abnormal behaviour is partially seen in high pass amplitude measurement. But in phase measurements they can be detected. These results suggest that, these abnormal behaviour can be corrected using high pass or low pass configurations, depending on the analyzed sample film impedance.

illumination, a surface photovoltage is generated and hence the surface potential changes. If, also, besides the photovoltaic change, the resistance and capacitance of the sample changes, there is an observed amplitude and phase change, which is usually the case. As a control example, an optical microscope slide is coated with Au/Pd and a resistor which is connected to the AC signal and a capacitor which is connected to the ground are connected to the Au/Pd layer. Then, by applying DC bias to the tip, amplitude and phase responses of first and second harmonics of the AC frequency is measured in the frequency range 160 Hz to 25 kHz. The setup used for this measurement is shown in Figure 2.9. DS345 is used as a frequency sweep. Either the first or the second harmonic's amplitude or phase is recorded together with the sweep output of DS345 simultaneously which is used as frequency axis. Amplitude and phase could not be recorded simultaneously because of the restrictions of the MFP3D controller, it has two DAC converters not used by standard configuration, and we use one of them for recording the frequency axis, i.e. sweep signal. Logarithmic triangular sweep is used in DS345. The measurements are quite repeatable. Especially, the abnormal changes around 2kHz and 20kHz are constantly seen, which we think to result from the MFP3D Asylum's input and output stage configurations. Other than these regions, the measured amplitude and phase responses depict the low-pass characteristics which should be the case. The electrical simulations done using circuit maker[2] are given in Figures 2.7(a) and (b). If the nodes we apply the AC and DC biases are interchanged, then without changing the measurement node, circuit becomes high-pass and shows the characteristics in Figure 2.7(c) and (d).

Staying within the limits that abnormal phase change of instrumental origin does not occur, we can observe the expected low pass or high pass circuit behaviour. As seen in the obtained amplitude and phase data, the data at every frequency stays in a certain limit. Therefore, obtaining the images of the same material at different frequencies, it is possible to extract approximate resistance and capacitance values.

Using this spectroscopic technique, surface photovoltage can be detected. Frequency sweep helps us to show that whether the impedance of the sample changes

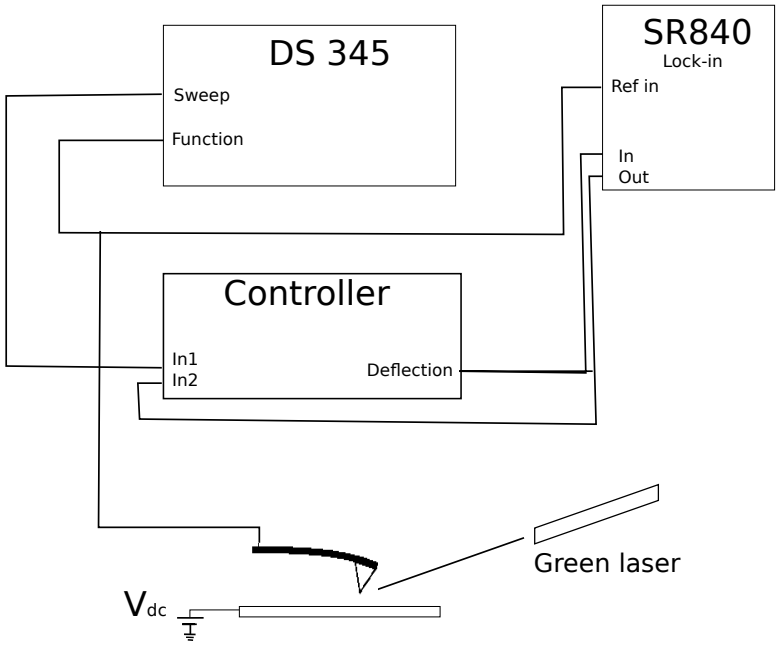

Figure 2.9: Measurement setup schematic for dynamical surface voltage measurements is shown. Green laser can be used for detection of illumination effect as done in Section 2.5, or other light sources can be used. Otherwise, no light source is used and frequency response is recorded as it is.

while illuminating with light. It may be possible that the nano or micro structure of the sample may change, such as grains may enlarge, grain boundaries may become more capacitive or resistive. Micro or nano structure change will result in change of total impedance. Grain boundaries were proven to show capacitive behaviour and hence in the case of micro or nano structure change, the impedance of the surface would change. This may result an increase of electrostatic force measurement and may not give the true surface potential. However, if the phase of the electrostatic force does not change, and we only see an increase of first harmonic of the electrostatic force, i.e. amplitude change, then either the impedance does not change, or film is very thin that contribution of impedance change is negligible. Hence, what is measured is the result of the surface photovoltage. The first harmonic of the electrostatic force is

$$F_\omega = \frac{1}{2}\frac{dC}{dz}(V_{dc} + V_s)sin\omega t \tag{2.29}$$

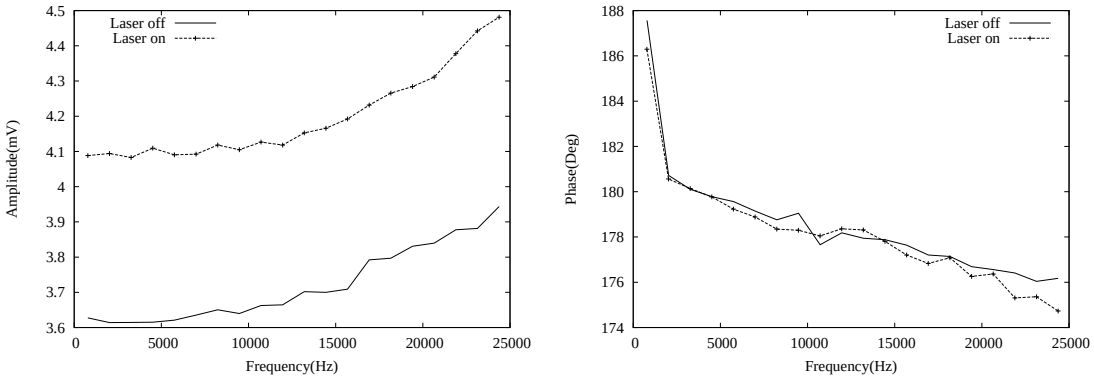

(a) (b)

Figure 2.10: In figure (a) amplitude of the first harmonic of the electrostatic force is shown for the laser on and off cases. There is a constant amplitude difference over the frequency range while the amplitude itself is not constant. In figure (b) there is no phase difference seen over the frequency range while the phase changes considerably for a single case. These two graphs indicate that, the change of impedance is negligible for the measured amplitude difference.

Therefore, for the phase not changing, but amplitude changing, the only way is the change of $V_{dc} + V_s$ term. Since we do not change the DC bias , surface potential (V_s) as a result of the illumination by laser should change. It is worth mentioning that the circuit configuration was high-pass circuit configuration and magnitude and phase responses show the same behaviour: magnitude increases as frequency is increased and phase decreases as in Figure 2.7(c) for magnitude and (d) for phase.

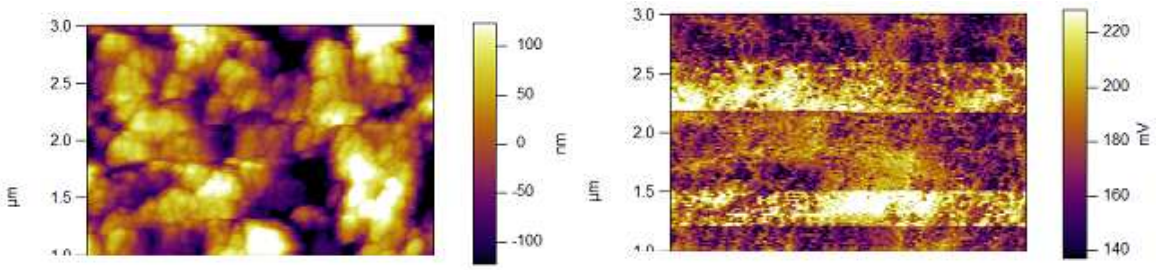

(a) (b)

Figure 2.11: (a) Topography of the CdS surface. (b) First harmonic of the electrostatic force image taken simultaneously with the topography. At the higher values seen in image (b), the laser is on. There is a clear amplitude difference, whereas no phase difference was observed. The images are taken at $\omega_0 = 5kHz$.

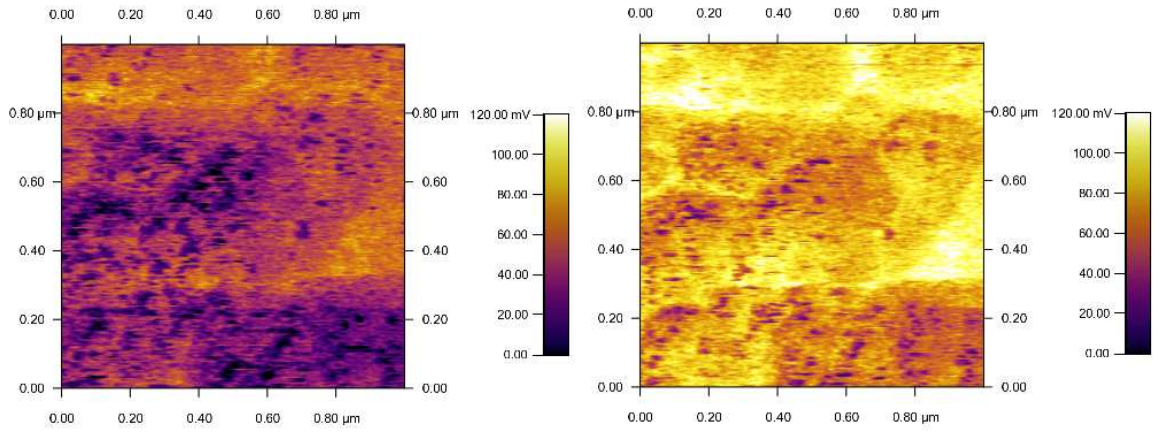

(a) (b)

Figure 2.12: First harmonic of the electrostatic force measured at $\omega_0 = 5kHz$ for the laser on and off cases. (a) Laser off case. (b) Laser on case. $V_{dc} = 1.0V$

Chapter 3

Tunneling current imaging and spectroscopy in contact mode

3.1 Description of tunneling between the tip and the sample

A rigorous formulation of the current can be modeled by the tunneling current, just as usually done in scanning tunneling microscopy. Starting from the Schrödinger's equation, we will denote the potential of the substrate and the tip as $V(\cdot)$ in the equation and solve wavefunction. Then, by the use of the matrix element current will be calculated.

$$i\hbar\frac{\partial\Psi_n}{\partial t} = \left[-\frac{\hbar^2}{2m}\frac{\partial^2}{\partial x^2} + V_s + V_{tip}(t)\right]\Psi_n \tag{3.1}$$

where V_s is the potential of the substrate and Ψ_n is the wavefunction of the nth state. Wavefunction has both spacial and time dependence. If it is assumed to be separable and forming a complete set denoted as $\Psi_n(x,t) = \Psi(x)e^{-iE_nt/\beta}$. Then the transition probability T_{nm} is

$$T_{nm} = \frac{2\pi}{\hbar}|M_{nm}|^2\delta(E_m - E_n) \tag{3.2}$$

where M_{nm} is the matrix element of the transition probability. It can be calculated by an integral

$$M_{nm} = -\frac{\hbar^2}{2m}\int(\Psi_m^*\nabla\Psi_n - \Psi_m\nabla\Psi_n^*)dS \tag{3.3}$$

The tunneling current is calculated by summing up over all possible electronic states. If the density of electronic states in the tip is ρ_{tip} and in the substrate is ρ_s,

$$I = \frac{4\pi e^2}{\hbar}V\rho_s(E_F)\rho_{tip}(E_F)|M|^2 \tag{3.4}$$

where V is the sample bias and E_F is the Fermi level. If only s-like functions contribute to the tunneling, then density of states of the tip near E_F is represented by,

$$\rho_{tip}(E_F)\ \alpha\ |\Psi_n|^2\alpha e^{-2\kappa(R+z)} \tag{3.5}$$

where R is the tip radius and z is the tip-sample separation distance. The decay length is,

$$\kappa = \sqrt{\frac{2m}{\hbar^2}\frac{(\phi_{tip} + \phi_{sub})}{2} - E + \frac{eV}{2}} \tag{3.6}$$

Since, tip is coated by a metal, current can be also written as,

$$I\ \alpha\ \int_0^{eV}\rho_{sub}(E)T(E, eV)dE \tag{3.7}$$

where $T(E, eV) = e^{-2\kappa z}$ is the transmission probability of the electron.

The passing current can be modeled by the tunneling current in the scanning tunneling microscopy. Here, exact calculation of the current is not necessary, but defining a proportional function that is dependent on the tip-sample distance is[21],

$$I\ \alpha\ \frac{CV}{z}e^{-2\kappa z} \tag{3.8}$$

I-V characteristics of a single point or an array of points can be measured using tunneling current microscopy. AFM is again driven in the contact mode.

Deflection is set to a constant level. After that, by varying the potential difference between the tip and the sample, current passing through the tip is measured. Semiconducting properties such as built-in potential, defining the contact type between a metal and the semiconductor where the metal is the coated metal on the tip may be determined or hysteresis behaviour can be observed.

3.2 Scanning Spreading Resistance Microscopy

Scanning Resistance Microscopy is done with a conducting tip, which is in repulsive contact with the surface for tip. The applied force is taken to be constant which is understood from deflection signal. Surface should make a good contact with the tip, possibly ohmic type. Conducting tip may be made by coating the tip by a highly doped, high strength material, like boron doped diamond, or a metal which enables a better electrical contact formation,e.g., tungsten[15] or any other suitable material. The schematic of scanning spreading resistance microscopy is shown in the Figure 3.2. A DC bias is applied between the tip and sample, and under constant deflection of the cantilever in contact mode, the passing current through the tip is recorded simultaneously with the topography signal. Usually a logarithmic amplifier is connected to the tip before the ampermeter to increase the measurable current range.

The spreading resistance and also the current passing through the tip depends on the effective contact area. The resistance between tip and sample can be calculated through

$$r = \rho/4a \tag{3.9}$$

where ρ is the resistivity of the sample and a is the contact radius. The contact radius is usually smaller than the tip radius, which enables better resolution[22]. The measured resistivity consists of a few parts.

$$R = R_{contact} + R_{bulk} + R_{tip} \tag{3.10}$$

The resistivity of the tip is neglected, since it is coated with a metal, which has a very low resistivity compared to the sample. Also bulk material has much larger

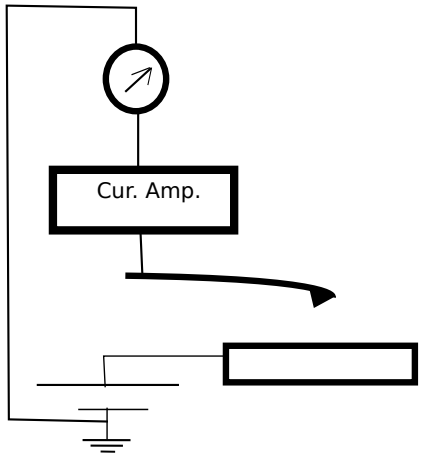

Figure 3.1: Schematic of SSRM. A DC bias is applied to the sample. The passing current is amplified and measured by an ampermeter and possibly the amplifier is a logarithmic amplifier to widen the measurable current range.

cross section area, so that its resistance can also be neglected. The dominant resistance is the resistance in the contact between tip and sample. The contact area depends on the tip and sample materials and the applied force between tip and sample. The greater the applied force, the greater the contact area and the higher the current signal. However, as usual, applying greater forces induces tip deformation.

Chapter 4

Applications to characterization of nanostructured surfaces

4.1 Electrical characterization and manipulation of properties of graphene

Resistivity is the intrinsic property of the materials. If in a single sample, there are two or many materials of different resistances, these can be distinguished by measuring their resistance. Then, analyzing the results, properties such as conduction mechanisms, the micro or nanostructure of the material can be found out. Besides, the charging of the materials can be quantized or at least the order of charging can be estimated.

In this section, scanning spreading resistance microscopy (SSRM) and electrostatic force microscopy (EFM) analysis of graphene, graphene oxide and partially reduced graphene oxide will be explained. Their structures were previously imaged in SEM[24]. Graphene oxide was synthesized using Hummers method[25]. Graphene was synthesized from it using thermal reduction. Graphene synthesizing can also be done by chemical reduction, such as by using hydrazine[26] or many other method that can be found in literature[41].

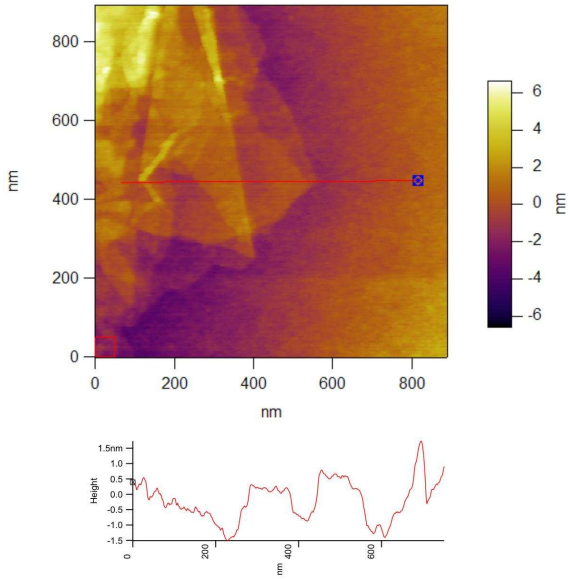

Figure 4.1: Topography image of a graphene sheet and a cross-section taken to measure thickness. It is about 0.5 nm, consistent with previous measurements found in the literature[27].

We have done characterization of the unrevealed electronic properties by SSRM. In SSRM, besides much better resolution of their structures, the conduction mechanisms were understood. Also, the reduction process was also partially imaged. Results of electrostatic force microscopy measurements were also combined by SSRM results. The thickness of the graphene layers were previously measured by different methods. One of the interesting ones is by reflection and contrast spectroscopy, which is very reliable due to the comparative measurements[27]. We also have measured the thickness of the graphene using contact mode operation. The sheets of graphene are distinctly visible so thickness can be determined roughly. In Figure 4.1, a graphene flake is seen. A cross section is taken to understand the thickness of graphene. The thickness is about 1.5 nm in general but 0.5 nm steps are also present which is near to the value Z.H. Ni *et. al.* measured[27].

4.1.1 Tip induced oxidation and reduction

Graphene is oxidized or graphene oxide can be reduced by different techniques. To make devices using graphene which is a semimetal is not enough, graphene oxide should be produced inside graphene and to do this, either graphene is oxidized or graphene oxide is reduced to tune open and also tune the band gap[33, 39]. Samples produced by chemical oxidation and reduction were characterized in detail using electrical characterization techniques[35–38, 42, 45]. High quality reversible techniques were found[46], so chemical control is also very promising. Especially using strongly reductive chemicals such as hydrazine, graphene oxide can be partially reduced to graphene. Changing the oxidation or reduction times[33] and temperatures[39] band gap can be tuned. Besides this, patterning graphene using lithography[37, 38, 40, 30], is possible by using e-beam lithography, optical lithography, nanoimprinting or laser induced imprint. However electrochemical reduction and oxidation are also important and a very good way to make electronic devices, since with these techniques, a few nanometers channel length , which is much smaller than the laser beam induced reduction[30], can be produced[32]. In a graphene/graphene oxide film, heterojunctions are formed and since these junctions and channels are not produced by doping differences, one does not need to think about diffusion of dopants, just as for the case of transistors made of silicon nanowires[31]. Therefore, electrical reduction and oxidation are promising techniques.

In Figure 4.2b, evidence of tip induced oxidation was observed. Under a potential difference between tip and sample, if the potential is enough, oxygen departs from hydrogen in water vapour molecules which are in the meniscus between tip and the sample, then oxygen bonds to graphene and forms graphene oxide, which is an insulator. We did not do oxidation in a complex shape, but evidence of oxidation while scanning a surface was provided.

In the reduction process, a serious difference can be realized. After scanning an area with a voltage pulse, not all of the scanned area was reduced, and the reduced surface was not filled by graphene, rather many islands and dots were formed as seen in Figure 4.2c. This suggests a slower process compared to the

oxidation case.

4.1.2 Characterization using tunneling current spectroscopy

The tunneling current changes exponentially as a function of tip-sample distance, and has a linear dependence on the potential difference. However, due to the material properties, the I-V characteristics may not be observed to be linear. Especially, if electrical current changes the chemistry of micro structure of the sample, the current may be exponentially dependent on the potential difference. Also, if a material that has a p-n junction was imaged, the current would be dependent exponentially to the potential difference. The tunneling current does not only depend on the potential difference and the tip-sample distance, but also dependent on the contact between tip and the sample. The formed contact is dependent on the work function of the materials. For there is a condition change in the surface of the sample, the tunneling current may increase or decrease, because the tunneling barrier changes. Also, formation of new surface states would change the density of states in the sample which would be seen as the change of tunneling current in the measurements. The reason why this latter change occurs can be understood from the Equation 3.4. Besides this case, illumination of the surface by a light source that will excite the surface electronic states changes the surface potential of the sample because of the accumulated charges, which is known as the surface photovoltage. This may change the conductivity considerably because the electrons or holes in the valence band for the non-excited case will be in the surface states. This may also be detected by tunneling current spectroscopy. The mentioned tunneling current differences are observed for graphene/graphene oxide samples. Illuminating by modulated white light source, the conduction is seen to change. Also, by reducing the graphene oxide by heating step by step, the tunneling current images seen to change. Furthermore, cyclic measurements of I-V on a single point for many times, an I-V curve showing hysteresis and many other electrical behaviours are seen. Photoconductivity for graphene was reported previously and mechanisms of generation and dissipation were discussed[34]. In our experiments, to explore the properties of graphene oxide, though quantification

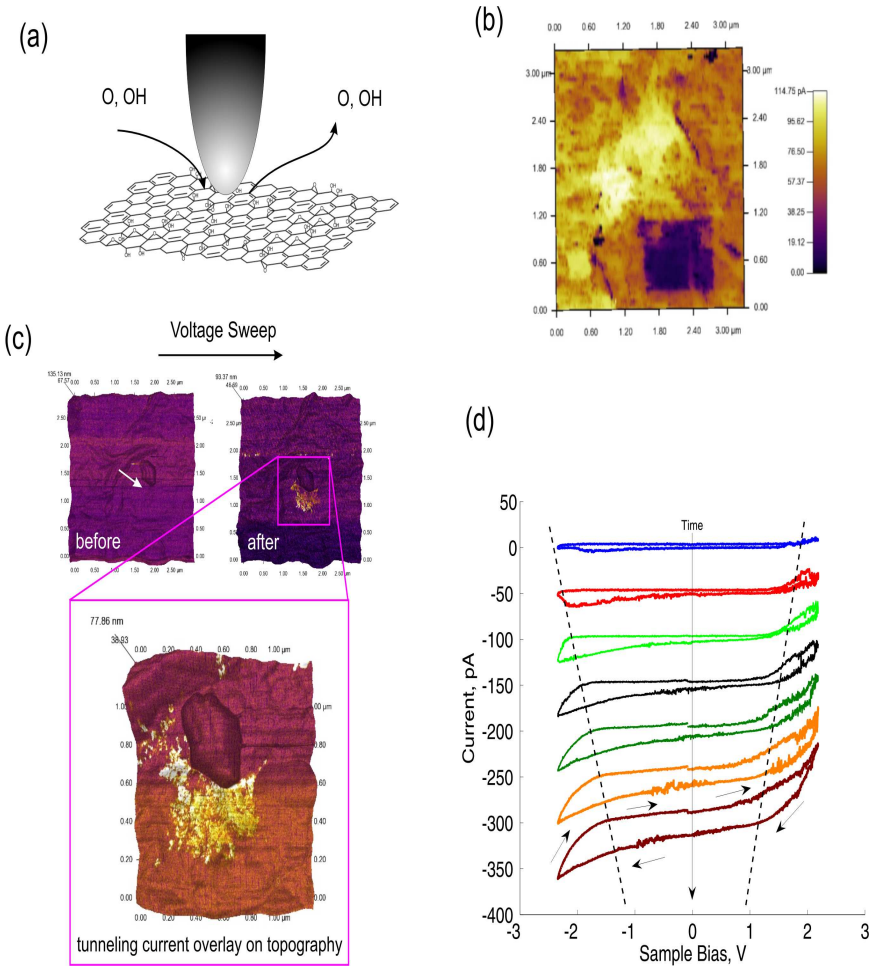

Figure 4.2: Tip-induced reduction and oxidation of graphene demonstrates that purely electrical routes are possible. (a) A conductive tip positioned over graphene/graphene oxide can be used to induce desorption of oxygen or oxidation. (b) Using a Pt coated tip, by applying a positive sample bias (2 V) oxidized regions can be written on graphene films. The tunneling current map, obtained with a 1mV bias shows a rectangular region that is oxidized by the tip. (c) A cyclic voltage sweep on graphene oxide (arrow) reduces a flake partially, resulting in conductive and insulating domains on the flake. (d) Current is monitored during the reduction process, showing the gradual narrowing of the band-gap of graphene oxide due to graphene inclusions. Despite a symmetric voltage sweep, a net reduction effect is observed, suggesting different mechanisms are dominant for the reduction and oxidation processes.

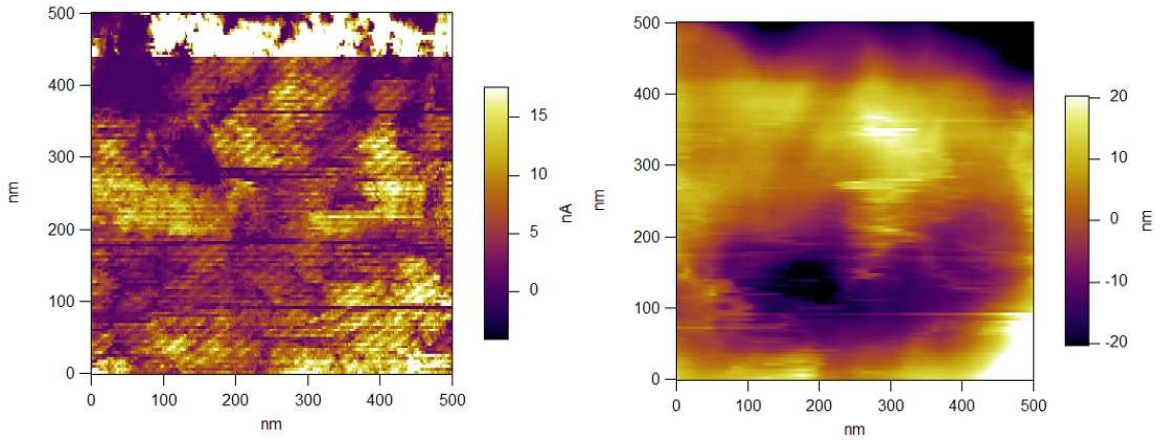

(a) (b)

Figure 4.3: Photoconductivity behaviour seen in the graphene oxide. A -25 mV pulse was applied on the film, which does not cause reduction. The sinusoidal signal seen in (b) has the frequency 50 Hz, which is the same frequency of the white light source.

was not done, the photoconductivity was observed. By applying a modulated white light source on to the graphene oxide sample, we have observed the photoconductivity. When light was completely turned off, there were no oscillations of current in the graphene oxide while imaging the tunneling current. But when light was turned on, the current was to oscillate approximately at the modulation frequency. Figure 4.3 shows the photoconductivity behaviour. The images were taken at a low electric bias (100 mV), so that micro or nano structure of graphene oxide was not changed by electrical means.

In order to understand the potential nanodevice applications, tunneling current measruements in different conditions can be done. By measuring the current using tunneling current imaging, the resistance (or conductance) of the surface can be imaged and by making a gate contact to the sample, potential of the materials for transistor applications can be explored. To understand a potential memory application of the graphene/graphene oxide, the application of different polarity of electrical pulses are applied for 10-15 seconds. For this experiment, a Au/Pd film on a SiO_2 sample was grown. The sample has two contacts of which the distance between them are $300\mu m$. Graphene oxide film was both on these contacts and between them on the SiO_2. A hard and a conductive tip was

prepared by coating a contact mode measurement tip by 30 nm of Pt. Applying potential difference between two ends of graphene oxide film causes reduction of the oxide, just as we have done in the nanoscale by a conductive AFM tip. The pulses are applied laterally between the contacts while the tip is retracted, and then while imaging the tunneling current, lateral bias is made 0 V and tip bias is made 100 mV. Then tunneling current image was taken. The images are shown in Figure 4.4.

As seen in Figure 4.4a, the initial sample of partially reduced graphene oxide showed little conduction previously pulses of changing polarity was applied and the last applied pulse was -2.5V. The reduced area, i.e. graphene dots or flakes, shows high tunneling current, but conducting area percentage is low. After the application of 2.5 V pulse, partially reduced graphene oxide was reduced more, and conducting area percentage increased. To check whether this process was reproducible, the same area was imaged multiple times and also a few micron nearby regions were scanned. Then we again applied a -2.5 V pulse. The tunneling current image showed that oxidation had taken place. But the process was not completely reversible as seen by the increase in the conducting area percentage compared to (a). These results suggest two things : 1- Graphene oxide was electrochemically reduced and oxidized and 2- The reason for the irreversible reduction was that there were short circuit paths formed between two contacts. In this way, after application of changing polarity of pulses many times, no change of tunneling current between opposite polarity pulses was observed. Because short circuit paths were formed between two contacts and the charges needed for oxidation of graphene cannot reach the domains between these paths. For the oxidation take place, there should be charge trapping in the conductive domains, which vanish when these conducting domains are interconnected.

These reduction and oxidation processes all happen at very low current levels and no significant topographical change occurs. This result suggests that the change of electrical properties occurs because of electrical means and not from mechanical changes made to the sample.

Reduction can also be seen in the I-V measurements. Measurement of I-V

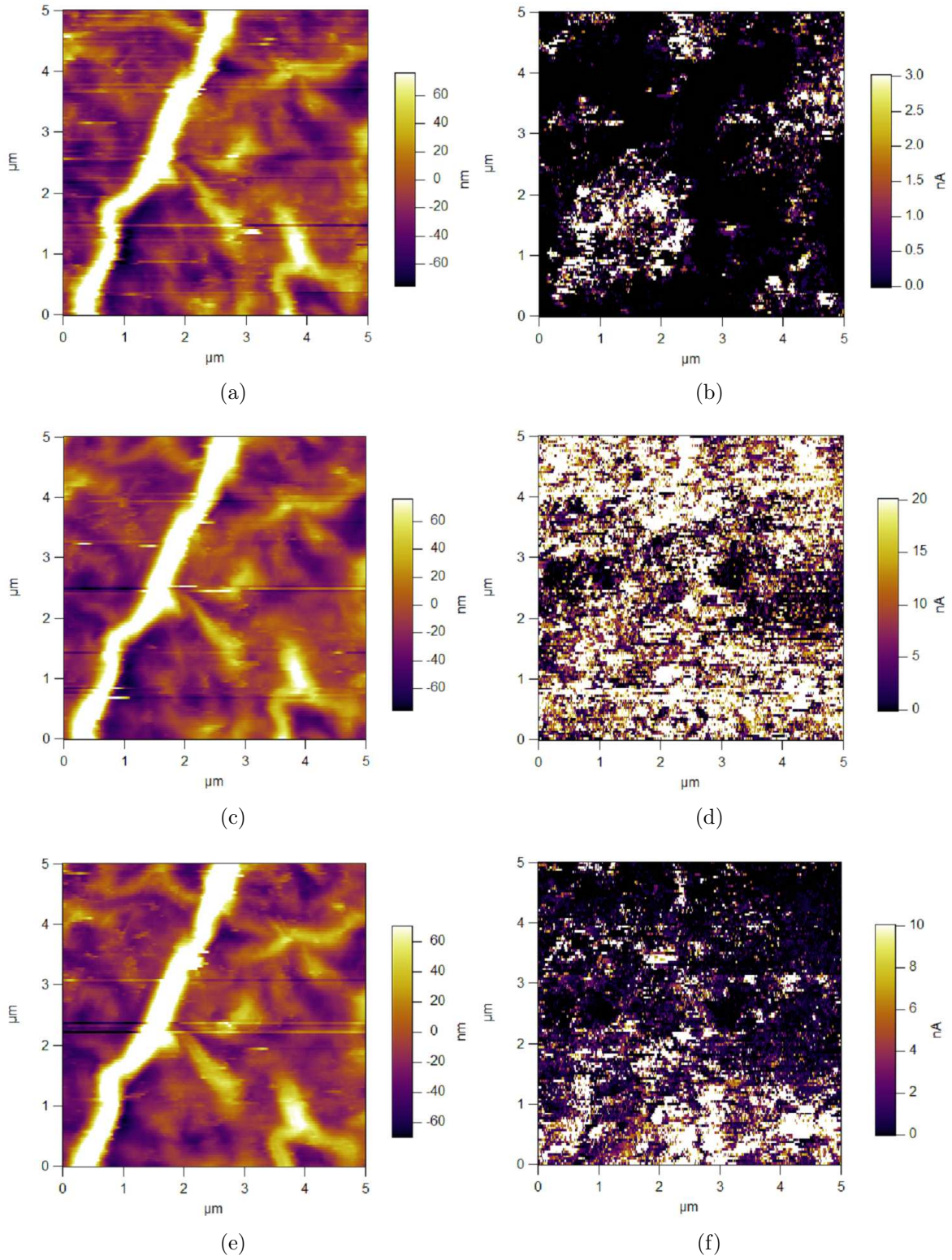

Figure 4.4: Figures (a),(c) and (e) show the topography measurements corresponding to current measurement in (b),(d) and (f) respectively. Applied bias while measuring the tunneling current is 100 mV. Figure (d) shows the tunneling current after application of a +2.5V pulse and (f) shows after application of a -2.5V. The duration of the pulses are 10-15 seconds.

before any application of high potential difference to the point I-V measurement is taken can be compared with the I-V measurement after application of a pulse or several I-V measurements of larger range I-V curves. Measuring the I-V first time on a point, the current level was seen to be low as seen in Figure 4.2d. After several I-V measurements of larger range potential differences, I-V measurements showed that conductivity increased a few times. The first current measurement showed hysteresis whereas after several I-V measurements hysteresis behaviour vanished which may be associated with irreversible reduction. However, this was not completely irreversible as we had only changed a small region's chemical structure and after application of DC bias to the film, we may observe that point was again oxidized which we had not experimented. But also there was a hysteresis behaviour as shown in Figure 4.2d. Note that these are not macro measurements. They were measured by tunneling current spectroscopy.

Also checking whether this process is reversible was done by applying a negative pulse for 10 s. It is seen that conduction area was decreased. The process was not completely reversible, but there was a little increase in the conducting area compared to the starting case. This is related to the hysteresis of the partially reduced graphene oxide. Hysteresis is shown in Figure 4.2d.

The widest gap in the hysteresis curve was measured to be 0.2V as shown in Figure 4.9. The double pass of the measurement shows clearly the same graphic except that a shift of 0.2V. This way of measuring hysteresis behaviour of materials were previously reported in Ref. [28]. These I-V hysteresis and electrostatic force hysteresis of graphene results from the following reason: Charge storage in graphene oxide islands results in reduction to graphene. Electrostatic force hysteresis shows the charge storage and I-V curve hysteresis shows the existence of reduction.

One of the studies we carried on the graphene oxide is the imaging of the conduction during the reduction process through heating graphene oxide. Figure 4.5 shows the SSRM image of the graphene oxide before the heating process started. The observed structure shows that there was a very little conduction that graphene oxide is effectively an insulator. Then heat was increased in 'ten'

steps. Because heating causes the cantilever to expand and bend and also affects the electronic components that control the x and y scanning offsets, the scanned area continuously changed. Therefore, we were not able to scan the same area on graphene oxide surface in every step and while the process was taking place. But after completing each step of thermal reduction process, we waited until the system becomes stable before imaging again, and multiple areas were scanned to get a good average representative map showing the effects of heating on graphene oxide in terms of reduction. The conduction started after heating to 100^o. Then increasing the temperature more, the conductive areas were observed to increase. As expected, there were flake structures in the image which are highly conductive, implying that graphene oxide was reduced to graphene. As seen, flakes were not connected in the view of charge transport in between the surface. Since this graphene-graphene oxide layer was thin, we may say that in every layer, there were flakes of graphene so that current conduction is either provided by the other neighbouring layers or tunneling of the charge carriers.

Currents greater than 20 nA cannot be captured by Asylum MFP-3D. A very high resistance about 1 GΩ is required to be connected in series, i.e. a shunt resistor or as explained in Chapter 3, a logarithmic amplifier is needed to widen the measurable current range. But we could not do that experiment. Currents greater than 20 nA should be understood as "a very large current" qualitatively.

Looking at the tunneling current maps, we see current plateaus. Currents are almost constant in this areas, passing through one plateau to another, we see a sudden drop of current. This suggests that, carriers see a resistance between these plateaus, which is the tunneling resistance.

Also, sometimes, there is a constant slope in the current passing through in one direction on many islands. The slope was observed to have same value in the high current islands and low current regions between these islands. Figure 4.7 shows topography and tunneling current images, and also the cross section that shows constant slope of current increment or decrement. This suggests that, some plateaus seen as a single large flake sometimes consists of much smaller graphene islands of a few nanometers which cannot be seen by available resolution at that

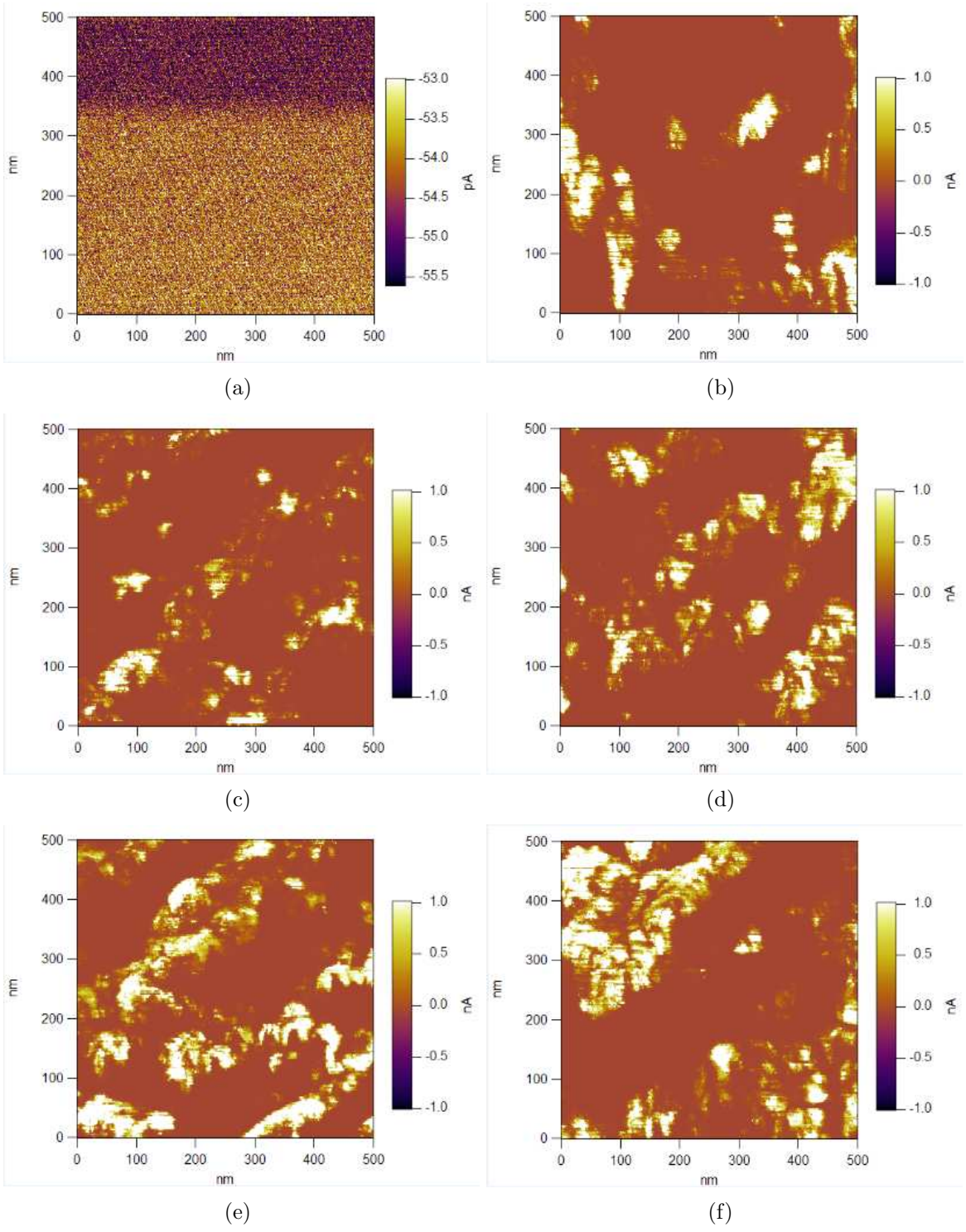

Figure 4.5: Heating process is shown step by step. a) Tunneling current map before heating. b) After conduction started. c-f) Different areas are scanned to assure the result.

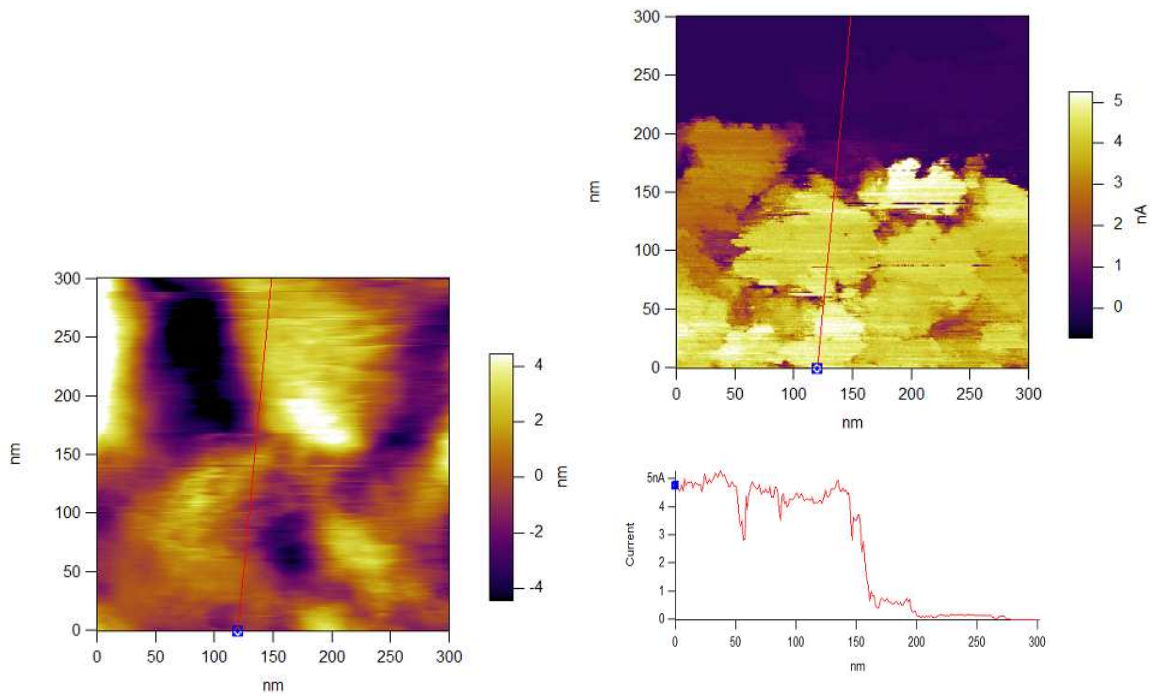

(a) (b)

Figure 4.6: Tunneling current images showing the current plateaus a) Topograhpy image and b) Tunneling current image. b shows many different constant current plateaus in the cross-section. This suggests that, the conduction mechanism is the tunneling between different current plateaus.

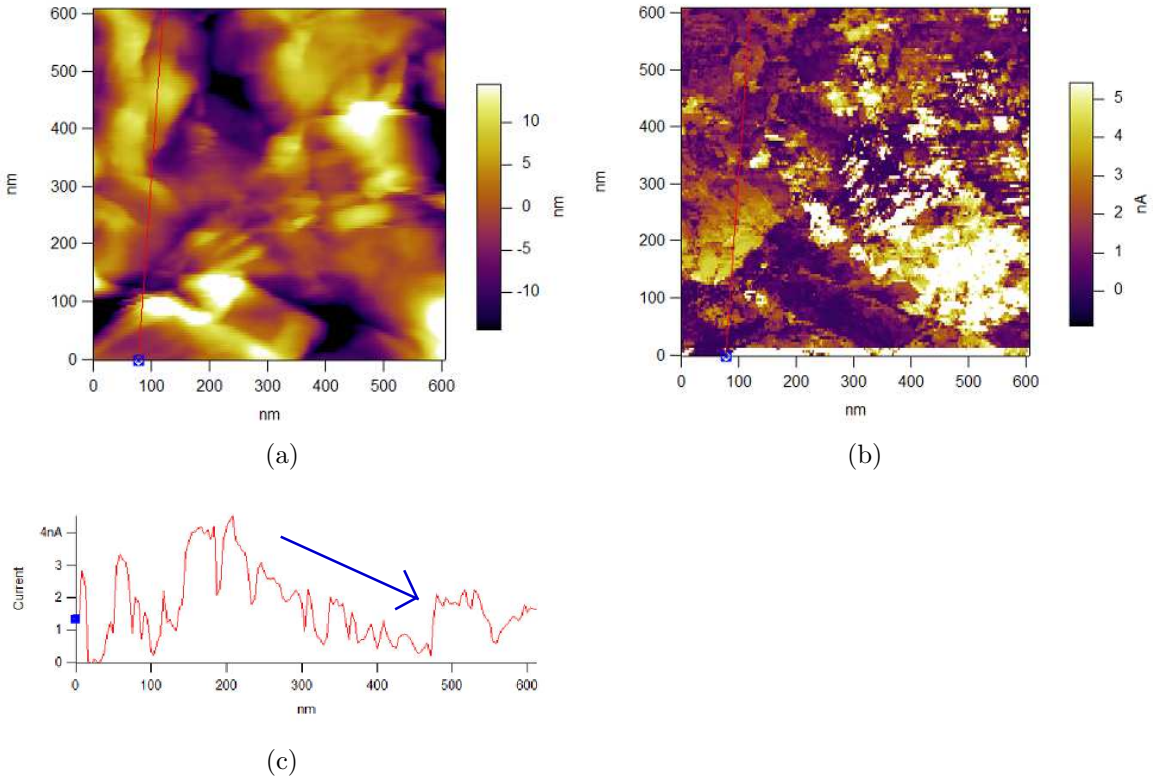

Figure 4.7: Tunneling current map of multilayer graphene film. Current shows a constant drop on the islands and between the islands. However we also see constant current plateaus.

measurement, so that a constant lateral resistance was observed.

By applying a higher bias number of current islands or quantum dots increased in graphene oxide. Whereas this shows the reduction of graphene oxide by electrical means, it also shows the difference of quantum dot formation energies depending on their sizes which was suggested in Ref. [29]. Scanning at a very low DC bias (50 mV), few number of dots were observed. There were distinct fall of current between those islands. Scanning at a higher DC bias (150 mV), more quantum dots were revealed. Taking a section from the image, we can be distinguish high current dot areas and in between them serious current drops. Therefore, the resolution is enough for the low bias case that we see less number of dots. Previously given reduction process in Figure 4.2c and in Figure 4.8 showed that scanning at a constant bias many times, number of dots did not

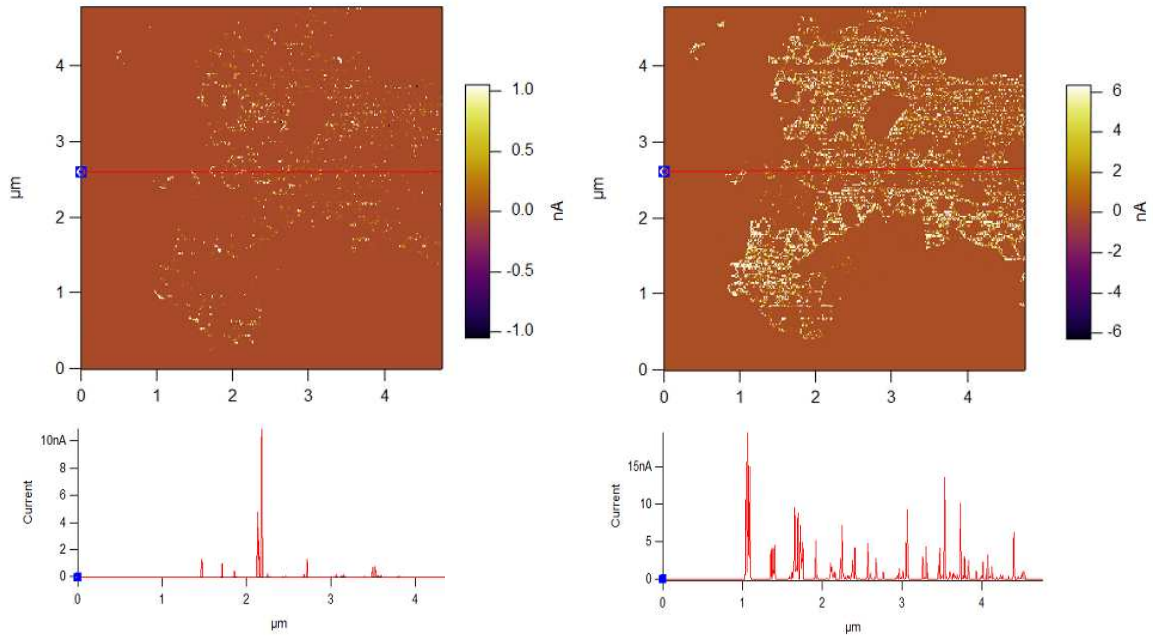

(a) (b)

Figure 4.8: Current section of nearly the same lines. a) Tunneling current map under $V_{dc} = 50mV$ and b) Tunneling current map under $V_{dc} = 150mV$. There is a certain increment in the number of dots, whose separations between them are also clear.

change significantly, so we can say that the dominant parameter in the change of number of dots is the value bias voltage and not the time.

4.1.3 Characterization using electrostatic force microscopy techniques

Measuring the surface potentials of the film reveals the different areas in the film. Since electrostatic force microscopy is known as low resolution method, especially in ambient conditions, obtaining a much better information about the material would not be possible by this method. However, using the special tip design as described in Section 2.1.1, the obtained resolution was shown to be better than 10 nm. Therefore, the nanostructure of the film was better understood. Electrostatic force microscopy enables the measurement of electrostatic forces between sample

and tip. The measured electrostatic force is related to the capacitance gradient and hence the dielectricity, also the tip sample distance and AC and DC biases. As written in Section 2.2.1, there were two harmonic components of electrostatic force. In the feedback driven system, the resulting cantilever oscillation amplitude is measured at constant driving frequency and constant driving amplitude. The electrostatic force time harmonic components were

$$F_w = \left[\frac{q_s V_{ac}}{4\pi\epsilon_0}\frac{C}{z^2} + C' V_{dc} V_{ac}\right] sin(\omega t) \tag{4.1}$$

and second harmonic was

$$F_{2w} = -\frac{1}{4}\frac{\partial C}{\partial z} V_{ac}^2 cos(2\omega t) \tag{4.2}$$

Charge storage results in the change of q_s, C and $\frac{\partial C}{\partial z}$ so that while applying voltage sweep, because of the charge storage, F_ω and $F_{2\omega}$ is shifted. The hysteresis can be also seen by electrostatic force spectroscopy. Since we apply a potential difference between the tip and the sample for the measurement of the electrostatic force, we can sweep the signal over a range of potential difference that includes oxidation and reduction processes of graphene, and also the two sides of the contact potential, we may try to observe the electrostatic force showing the hysteresis behaviour. In this measurement we have done a double pass measurement over the sweeping range each time, just as Bostanci et al. experimented [28] and controlled the repeatability of the observation by repeating the measurements.

In Figure 4.10a and b, first and second time harmonics of the electrostatic force images are shown. Comparing these images with Figure 4.10c and 4.10d, no correlation between topographical image-phase image and the electrostatic force images can be seen. This demonstrates that there are no couplings between these two groups of measurements, which were measured simultaneously. In Figure 4.10, one edge of the images are 100 nm. The color scale are shown next to each image. Electrostatic force images reveal very fine electrical details which are not found in topographical image. The size of the smallest features are smaller than 10 nm, with distinct borders around it. In Figure 4.10a, the sample bias

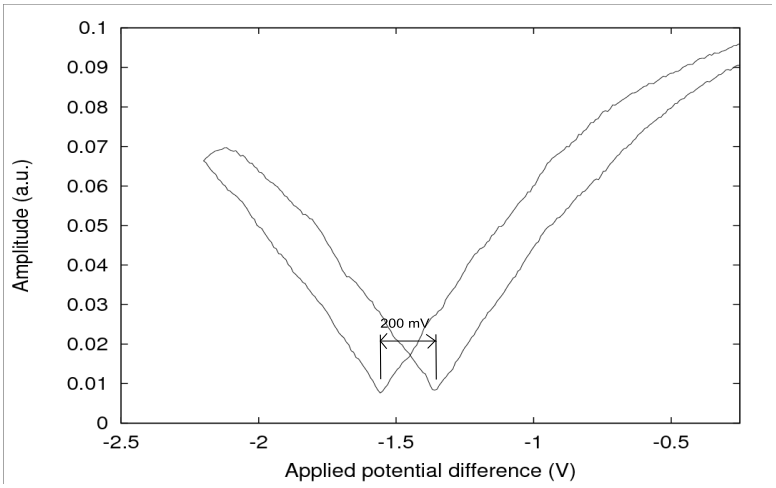

Figure 4.9: Amplitude of the first time harmonic of electrostatic force with changing DC bias. The two way sweep over the bias range shows a shift of about 200 mV shift, which is an evidence of hysteresis.

voltage was 1 V and in 4.10b, it was 0.5 V. While the topographical image does not change (not shown in the figure), the electrical force image changes. The signal level difference between maxima and minima in Figure 4.10a is about 300 mV, while in Figure 4.10b it is about 240 mV. The ring shaped bright edges express the high correlation of bias voltage and the electrostatic force images. The thickness of the rings are smaller than 10 nm, as seen in both Figures 4.10a and 4.10b, which demonstrates the resolution capability. Having a very high electrostatic force resolution in both surface potential images (first time harmonics) and tip-sample capacitance images (second time harmonics), we can trust the results that can be inferred from the images. As seen in comparison of Figures 4.10a and c shows that a large graphene oxide domain (seen as the brighter region in the left) is split into two parts by formation of a graphene channel in between them by application of a higher bias. Even without changing the bias, reordering of the distinct surface potential domains can be seen as seen in Figure 4.11. The results show that there are distinct surface potential domains on the graphene oxide domains. This is a result of bonding of different functional groups. % 100 or % 0 coverage is not stable as suggested in the theoretical works[43, 44]

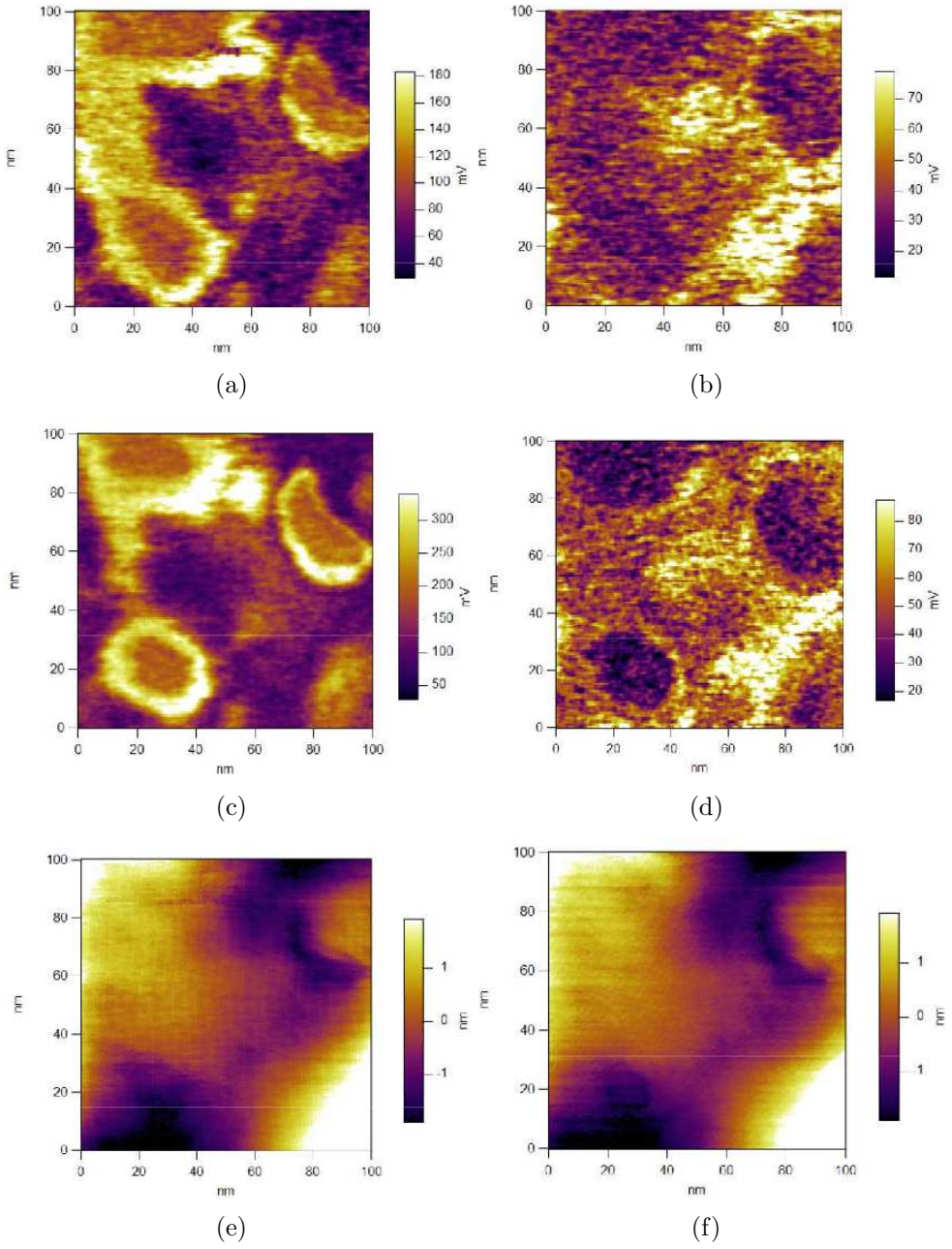

Figure 4.10: Electrostatic force microscopy measurement using two harmonics. The images illustrate the resolution achieved using the special tip design. Also the reduction of graphene oxide by the application of an electric field without any tunneling current is seen (a,c) First and second time harmonics of the electrostatic force which corresponds to surface potential images taken at lower DC bias. (b,d) Same measurement at a slightly higher bias, (e,f) Topography images for the two images Looking at e-f, we do not see the details that we see in a-d, which shows that those differences belong to an electrical property, namely surface potential and tip sample capacitance. Brighter regions in a and b show the higher surface potential areas (graphene oxide). In figures (a) and (c) a large graphene oxide domain (brighter region in a) is seen. After imaging under an electric field of about 0.5V/nm, this large domain is splitted into two domains by formation of a graphene channel. Capacitance images in figures b and d shows the opposite contrast,i.e. darker regions correspond to graphene oxide.

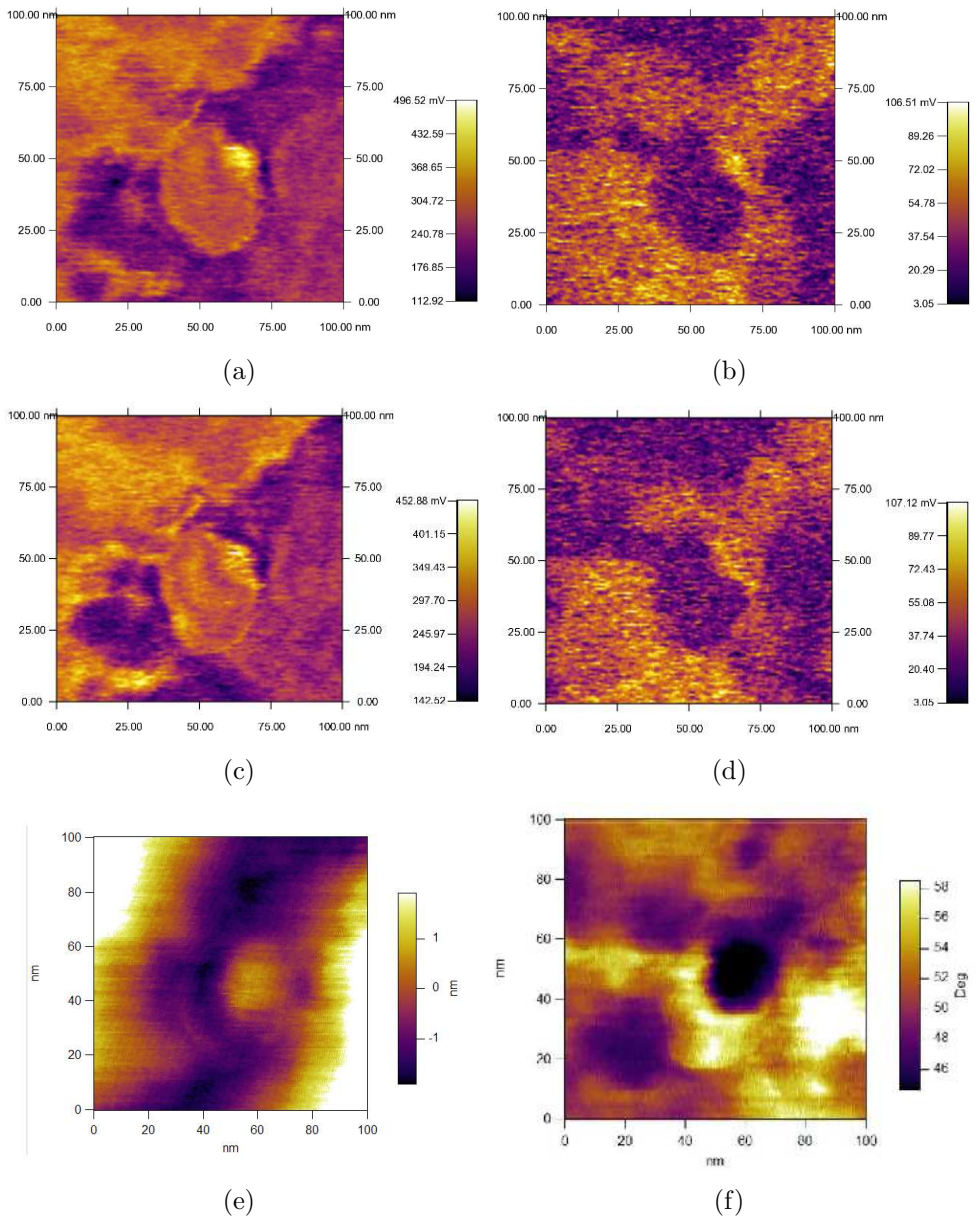

Figure 4.11: Electrostatic force microscopy measurement using two harmonics showing the effect of applying electric field and the variations of the graphene oxide domain inside itself over time. a) First harmonic of the electrostatic force. b) Second harmonic c) Immediately following remeasuring of first harmonic of the electrostatic force on the same area. d) Second harmonic e) Topography image f) Phase image. The topography and phase images did not change over time, whereas the surface photovoltage and capacitance images are seen to be changed. There are many regions of different surface potentials and capacitances in the bright region, whereas dark regions show almost no variation. This shows that graphene oxide surface consists parts that are bonded in different configurations.

Chapter 5

Future prospects

In the scope of high resolution electrostatic force imaging, we have set a goal on plasma induced defects in photonic crystals and understanding the effects of it. This chapter describes the fabrication and preparation of a many-device for analysing under EFM. Although the preparation has been completed, due to the maintenance problems in FIB, we could not produce the tips that we have explained in Chapter 2.

5.1 GaN light emitting diode with a plasma etched photonic crystal

5.1.1 Sample preparation

Preparation of LED devices includes both standard LED preparation except packaging, etching the photonic crystals, preparation of macro contact sample to use with EFM equipment for biasing LEDs that will be analysed by EFM and wire bonding from the LEDs to this macro contacts. The process flow is shown in tabular form in Table A.1. In the first step, p-metal contacts are done by optical lithography and lift-off. 5 nm/5 nm Au/Pd layer is deposited for p-metal. As

the lithography resist, AZ5214E is used. For negative lithography, 100 mJ/cm^2 exposure is done. Reversal bake is done at 120^oC for 2 minutes. Flood exposure dose is slightly over 200 mJ/cm^2 and duration of developing is 45 seconds. Annealing of p-metals is not done at this step. This layer is used for alignment in e-beam lithography step for the photonic crystals.

Then a layer of 90 nm SiO_2 deposition is done by sputtering as a hard etch mask for photonic crystals. The growth rate is about 0.5 nm/s. RF power is 60 W and Ar flow is 25 $sccm$. After that e-beam lithography is done on mask layer. PMMA 495K A2 solution is used as a resist. It is spinned on the sample at 3000 rpm, which results in $\approx$ 60 nm film thickness. After that photonic crystal structures are exposed in the e-beam lithography. Both square lattice and triangular lattice structures are built. The calculated dimensions for photonic crystal etched rods were 260 nm and 430 nm in diameter[23], but square structures instead of circles were exposed and the shape and diameter of the structures were calibrated by changing the dose. The spatial period is 520 nm for both lattice structures. The exposure parameters change according to the diameter and the number of nearest neighbor points. For greater diameter and greater number of nearest neighbor lattice points, lower doses should be applied. That means, for structures that have greater diameter and edge length, lower doses should be used to prevent overexposure. Also, square lattice has four nearest neighbours whereas triangular lattice has six nearest neighbours.Therefore, for triangular and square lattice 260 nm structures, 90 $\mu A/cm^2$ is applied. Maybe dose should be decreased $3-4$ $\mu A/cm^2$ for triangular lattice, but that is not applied as it makes little difference. For the triangular lattice of diameter 430 nm, the dose is 72 $\mu A/cm^2$ and for the square lattice 66 $\mu A/cm^2$. The same dose is applied for the box shape 430 nm edge structures. The reason that one edge is 380 nm is that, the area of that box is nearly equal to the area of the 430 nm diameter.

Next, reactive ion etching (RIE) of photonic crystals are done. Firstly, PMMA is hard baked at 100^oC on hotplate for 2 minutes. In this way, PMMA can withstand nearly 4.5 $mins$ etching,i.e. at an etch rate of less than 15 nm/min, in CHF_3 plasma. The RIE parameters are 100 W RF power, 26 μbar pressure and 20 $sccm$ CHF_3 gas flow rate. SiO_2 etch rate in CHF_3 plasma is $23-24$ nm/s

and therefore the photonic crystal structure in PMMA is passed to SiO_2 mask layer in a slightly amplified depth, whereas diameters do not change much. Then, again using RIE, etching the photonic crystal structures into GaN is done. The etching parameters are 100 W RF power, 20 $sccm$ gas flow rate and 8 μbar pressure. GaN etch rate is found to be $25 - 30$ nm/sec whereas SiO_2 etch rate is smaller than 20 nm/sec. Therefore, after 3.5 $mins$ etching in CCl_2F_2 plasma, GaN is etched about $90 - 100$ nm, whereas SiO_2 is still left above 10 nm for safety. Then, SiO_2 is removed.

After that annealing of p-metal layer is done for 3 min at 500^oC by rapid thermal annealing (RTA). After that,n-metal and pad metal lithography is done. Procedure is the same except for negative exposure and reversal bake steps. Deposition of metal are done by lift off. 20 nm/450 nm Ti/Al metal is deposited. Annealing is not done for these steps.

In the next step the macro contact sample is prepared, and then the prepared GaN LED is put into this macro contact sample. Macro contact sample is a printed circuit board (PCB) made from epoxy filled fibreglass coated by a thick Cu layer on one side. An acetate mask was prepared for lithography which is shown in Figure 5.1, and $1 : 1 : 6$ parts of 30% H_2O_2 : 37% HCl : H_2O is used as an etchant. After that, ball bonding is done. Au (gold) wires of 25 μm thick is used. Processing temperature was 110^oC. Making a bond on a copper may not be reliable, especially if bonding will be done many times. It was necessary for our work to make bonding not at a single time for preparing sample for EFM measurements, because if there are many bonding wires, we would not be able to get down to the surface without hitting to one of wires, which is still difficult when there are is a single wire because of the depth of focus of the EFM optical configuration. Also depositing aluminum layer over the copper layer was tried as Chu-Chung Lee and coworkers have done [47]. To prevent diffusion between aluminum and copper under high temperature greater than 100^oC titanium diffusion barrier layer is grown. This is because if the diffusion happens, the bonding pad is degenerated mechanically. The thickness of the titanium layer was 50 nm whereas aluminum layer is 700 nm. Ball bonding over aluminum bonding pad with Au (gold) wires is more reliable compared to copper

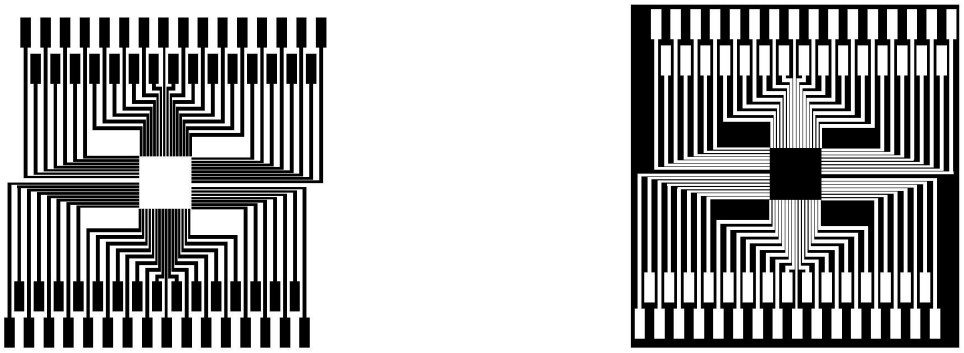

Figure 5.1: Figure shows the masks for use in the wire bonding of LED contacts to larger contacts. These wire bonds are needed to place PC LED structures into the AFM system for electrical characterization

bonding pad. But, as observed many times, depositing so thick an aluminum layer is problematic, the resulting film may not be a good film because of the surface of Cu on PCB and the crucibles used for Al evaporation. As a result Al deposition, we have seen that the capillary was clogged by aluminum particles after a while and cleaning procedure should be applied very often, which makes bonding procedure interrupted many times and very long. For a good result, aluminum should be grown in a good quality. Therefore, later, although we continued to make bonding multiple times, we used the bare copper surface. We have seen that, 450 nm Al layer in the LED pad contacts were very reliable after many times heating for wire bonding, whereas PCB had to be changed over that time for bonding procedure became cumbersome. Completing these steps, the sample is ready for analysing under EFM.

5.1.2 Imaging

Measurement of the tip we have prepared shows excellent measurement of topography. We have also shown the high electrostatic force image resolution. We want to combine these two features. Although we could put the sample under AFM, and measured the topography again with a slightly worn tip that was fabricated as described in Section 2.1.1. Because of the time considerations and maintenance problems in focused ion beam (FIB), we could not fabricate a new tip and

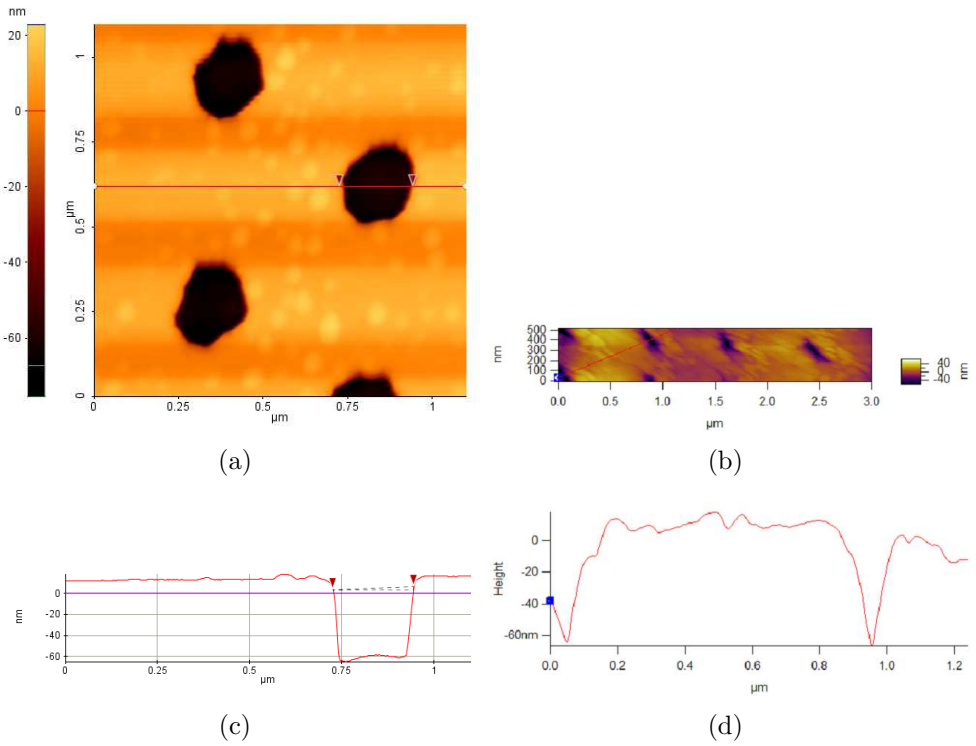

Figure 5.2: Demonstration of the tip's capability of topography measurement. The depth of the structure is 70 nm, and the width is smaller than 180 nm. The measured wall angle is approximately 80^o.

measure the electrostatic forces in high resolution. But our aim is to analyse these fabricated LEDs under EFM for understanding the surface states, defect states on a sample that is very difficult to analyse by EFM. Even topographical measurement in such a structure may not reliable. But the tips we have used excellent performance. Figure 5.2 shows that photonic crystals can be measured by this tip. Measuring high wall angle up to 80^o in well narrower than 180 nm and having a 70 nm height. Measuring higher depths is also possible but maybe a wider structure is necessary, which we did not test. For comparison, topography measurement data using a slightly worn tip is shown in Figure 5.2 (b),(d) . As seen, the depth cannot be seen, which was previously measured to be over 90 nm, and the angle between the wall and the surface are very small, which was not the case.

In Figure 5.3a, a picture taken from Asylum MFP-3D AFM setup camera,

that shows the prepared GaN LED with its wire bond contacts and ready to scan with AFM probe. The comparison of the light extraction between two LEDs with photonic crystals shows a considerable light extraction difference (Figures 5.3b and d). It would be a good experiment to analyze the electronic origin for this extraction difference.

5.2 Graphene devices using oxidation and reduction

The reason for working on graphene/graphene oxide oxidation/reduction would not be clear if potential device applications are not mentioned. Isolating these devices from open air and water vapour, application of a potential difference would not cause further reduction or oxidation. Using the charge storage capability as demonstrated by the hysteresis curve obtained from electrostatic force microscopy (EFM) results as shown in Figure 4.9, an isolated graphene island may store charges, whereas the graphene channel may be used for transporting the charge carriers, and another graphene island can be used as a gate as shown in Figure 5.4(b). Since the available channel length by using a scanning probe tip can be much smaller than today's channel length used in CMOS technology, smaller devices can be constructed. Silicon nanowire transistors were previously done, and since they do not have junctions, like in graphene/graphene oxide case, easiness in fabrication and applications were discussed[31]. Another application would may use electron wave interferences as a switch as shown in Figure 5.4a. As a ring resonator used in optics, this configuration can be used in electronic devices, whose dimensions should be small because electron has a much smaller wavelength compared to visible wavelength photons.

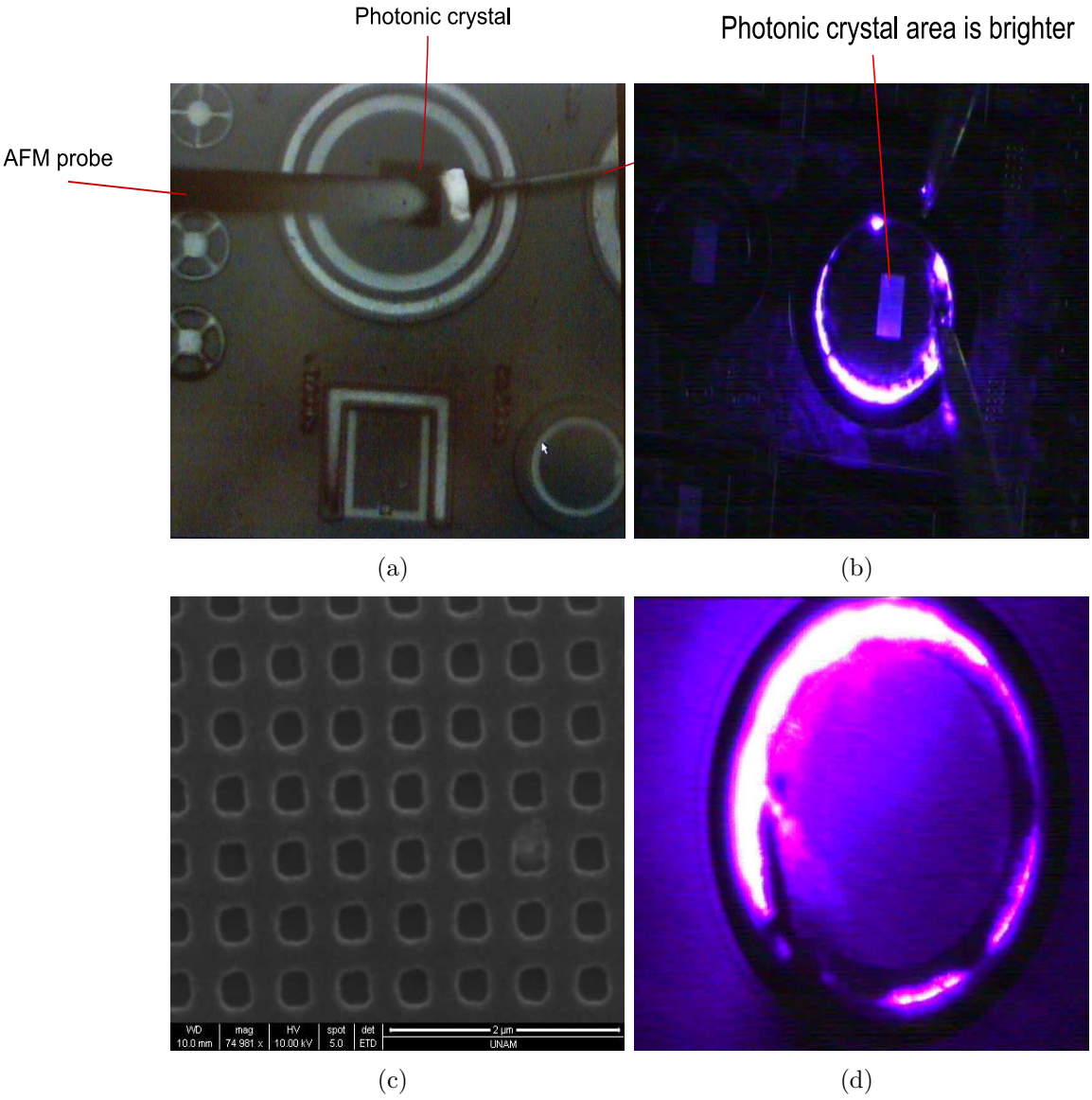

Figure 5.3: (a) Demonstration of the AFM measurement setup on the AFM camera. There is photonic crystal under the AFM tip, and the wire coming from the right is the gold wire. (b) Demonstration of the effect of photonic crystals on the light distribution at a low bias current (300 μA). (c)SEM image of the photonic crystals when there is still PMMA on the surface.After etching, SEM imaging would degrade the LED electrical performance. (d) A lighting LED with a photonic crystal which does not show any improved light extraction as the photonic crystal area cannot recognized.

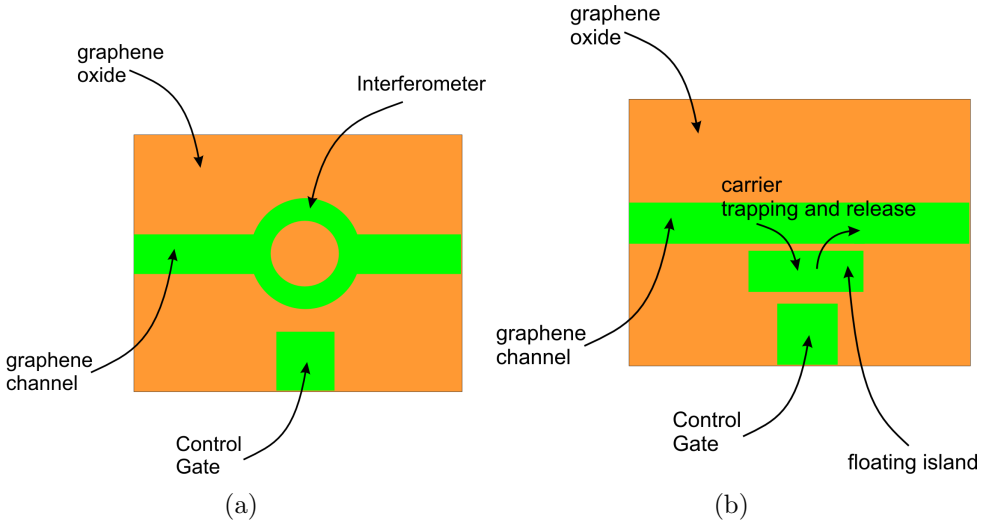

Figure 5.4: (a) An electron interferometric switch is shown as a schematic. (b) A potential memory application consisting of a field effect transistor which is made by forming a graphene channel inside graphene oxide film by tip induced reduction.

Chapter 6

Conclusion

In this work, high resolution electrostatic force microscopy together with scanning spreading resistance microscopy is applied to find out electrical characteristics graphene and graphene oxide samples. Surface of graphene oxide is shown to consist of different functional groups as can be understood from surface potential images. The hysteresis behaviour of graphene is observed both by taking I-V curves at a single point using SSRM setup and EFM setup using bias sweep. The reasons for hysteresis is seen to result from reversible reduction and oxidation. And the reason for diminishing hysteresis characteristics is stemming from irreversible reduction of graphene oxide, which is a result of shorting paths formed between two electrical contacts after many times reduction and oxidation. The reasons for obtaining simultaneous high contrast first and second time harmonic images in EFM is explained in terms of tip desing, as the tip design prevents mechanical oscillations and instabilities and also reduces the contribution of tip bulk to the tip-sample capacitance change. Impedance spectroscopy imaging using EFM is demonstrated and applied to surface photovoltage detection in CdS samples. Pure surface photovoltage measurement is demonstrated by unchanging phase spectrum and a considerable change of magnitude spectrum in first time harmonics of electrostatic force.

Appendix A

LED processing flow

1	**Cleaning**
	– ACE and ISO in ultrasonic for 2-3 mins
	– Blow in dry nitrogen
	– Dry in hotplate at 110^{o}C.
2	**p-Metal contacts**
	p-Metal lithography
	– Spin AZ5214E resist at 5000 rpm for 40 sec
	– Bake at 110^{o}C for 50 sec.
	– Expose for 30s in 3.2 mW/cm^2 UV source
	– Reversal bake at 120^{o}C for 2 mins.
	– Flood exposure for 70 sec
	– Develop for 45-50 sec in AZ400K:DI 1:4
	– Rinse in DI for 90 sec
	– Dry with N_2 gun.
	p-Metal deposition
	– HCl:DI 1:3 dip for 1 min, rinse in DI for 1 min
	– Dry with N_2 gun.
	– Deposit Pd/Au (5 nm/10 nm)
	p-Metal lift-off
	– Wait for 30 min in 55^{o}C ACE
	– In ACE, use ultrasonic for 15 sec.

	– Dip in ISO, rinse in DI
	– Dry with N_2 gun.
3	**SiO_2 deposition**
	– 90 nm SiO_2 sputter in 25 sccm Ar flow, 60W RF power
4	**Photonic crystal**
	E-beam lithography
	– Spin PMMA 495K A2 resist at 3000 rpm for 45s
	– Bake at 180^{o}C for 90s
	– E-beam exposure dose of 66-94 $\mu As/cm^2$, specified according to feature diameter
	– Develop for 30s, rinse in stopper for 30s
	– Dry with N_2 gun.
	RIE etch
	– Hard bake at 100^{o}C for 2 min
	– Etch SiO_2 mask in 20 sccm CHF_3 flow, 26 μbar, 100W RF power for 4.5 min
	– Etch GaN in 20 sccm CCl_2F_2 flow, 8 μbar, 100W RF power for 3.5 min
	– Clean in ACE 10 min in 55^{o}C ACE.
	– Dip in ISO, rinse in DI
	– HF:DI 1:50 for 5 min to etch SiO_2 completely
	– Rinse in DI
	– Dry with N_2 gun.
5	**Annealing p-Metal**
	– Anneal in RTA for 3 min at 500^{o}C
6	**p-Metal contacts**
	n-Metal and pad metal lithography
	– Spin AZ5214E resist at 5000 rpm for 40 sec
	– Bake at 110^{o}C for 50 sec.
	– Exposure for 70 sec

	– Develop for 45-50 sec in AZ400K:DI 1:4
	– Rinse in DI for 90 sec
	– Dry with N_2 gun.
	n-Metal and pad metal deposition
	– HCl:DI 1:3 dip for 1 min, rinse in DI for 1 min
	– Dry with N_2 gun.
	– Deposit Ti/Al (20 nm/450 nm)
	n-Metal and pad metal lift-off
	– Wait for 30 min in 55^{o}C ACE
	– In ACE, use ultrasonic for 15 sec.
	– Dip in ISO, rinse in DI
	– Dry with N_2 gun.
7	**PCB making**
	PCB Lithography
	– Spin AZ5214E resist at 150 rpm for 10s and at 1500 rpm for 45s
	– Bake at 110^{o}C for 60s.
	– Exposure for 75s
	– Develop for 45-50s in AZ400K:DI 1:4
	– Rinse in DI for 90 sec
	– Dry with N_2 gun.
	Metal etch
	– 30% H_2O_2:37% HCl:DI 1:1:6 dip for several minutes, rinse in DI for 1 min
	– Dry with N_2 gun.
	– ACE clean with ultrasonic for 2 min
	Wire bonding
	– Drill the place for LED
	– Do wire bonding at 105^{o}C using 25 μm diameter gold wires.

Table A.1: LED processing flow for preparation of GaN LEDs to examine its optoelectronic properties using Atomic Force Microscopy (AFM)

Bibliography

[1] M.S. Lheurnold *et al.*, Appl. Surf. Sci. **253** 6203-6210 (2007)

[2] http://my.ece.ucsb.edu/bobsclass/2C/Simulation/circuit_ maker.htm

[3] Ding *et al*, APL **94**, 223109 (2009)

[4] M.K. Abak *et al.*, Appl. Phys. Lett. **92** 223113 (2008)

[5] S. Gomez-Monivas *et al.*, Nanotechnology **12** 496-499, (2001)

[6] Dror Sarid, Scanning Force Microscopy Rev. Ed.,Oxford University Press,(1994)

[7] D.F. Ogletree, R.W. Carpick, M. Salmeron, Rev. Sci. Instrum. **67**, 3298-3306 (1996).

[8] M. Varenberg, I. Etsion, G. Halperin, Rev. Sci. Instrum. **74** 3362-3367 (2003).

[9] A. Avila, B. Bushan, Critical Reviews in Solid State and Materials Sciences, **35** 38-51, (2010)

[10] S.V. Kalinin and D.A. Bonnell, Appl. Phys. Lett., **78** 9, 1306 (2001)

[11] R.Shao,S.V. Kalinin and D.A. Bonnell, Appl. Phys. Lett., **82** 12, 1869 (2003)

[12] S.Krause *et al.*, Electrochimica Acta, **51**, 1423-1430 (2006)

[13] S.V. Kalinin and D.A. Bonnell, Mat. Res. Soc. Symp. Proc, **699**, R1.2.1-6 (2002)

[14] M. Freitag *et al.*, Phys. Rev. Lett., **89** 216801, (2002)

[15] E. Meyer, H.J. Hug, R. Bennewitz, Scanning Probe Microscopy:lab on a tip, Springer Berlin, New York (2004)

[16] C. Ballif *et al.* J. App. Phys. **89** 2, 1418 (2001)

[17] C. Jiang *et al.*, Appl. Phys. Lett. **81** 14, 2569 (2002)

[18] D. Douheret *et al.*, Microelectronic Engineering **84**,431-436 (2007)

[19] J.N. Barisci *et al.*, Synthetic Metals **124**,407-413 (2001)

[20] A. Alexeev, J. Loos, M.M. Koetse, Ultramicrsocopy **106**,191-199 (2006)

[21] H.J.W. Zandvliet and A.V.Houselt, Annu. Rev. Anal. Chem. **2**:37-55 (2009)

[22] X. Ou *et al.*, Nano Lett., **10**,171-175 (2010)

[23] A.G. Kaya, Bilkent University, M.S. Thesis to be submitted to Graduate Program of Materials Science and Nanotechnology (2010)

[24] O.Ö. Ekiz, Bilkent University, M.S. Thesis to be submitted to Graduate Program of Materials Science and Nanotechnology (2010).

[25] W.S. Hummers and R.E. Offeman, J. Am. Chem. Soc. **80** 6, 1339 (1958)

[26] S. Chandra, S. Sahu and P. Pramanik, Mat. Sci. and Eng. B **167**,133 (2010)

[27] Z.H. Ni *et al.*, Nano Letters **7** 9, 2758 (2007)

[28] Bostanci et.al. , Appl. Phys. Lett. **92**, 093108 (2008)

[29] A.K.Singh,E.S.Penev,B.I.Yakobson, ACS Nano**4** 6, 3510 (2010).

[30] Y. Zhang *et al.*, Nano Today **5**, 15-20 (2010)

[31] Colinge et. al., Nature Nanotechnology, **5**, 225 (2010)

[32] Z.Wei *et al.*, Science, **328** 1373 (2010)

[33] H.K. Jeong *et al.* J.Phys.D.:Appl.Phys. **42**,065418 (2009)

[34] J.Park,Y.H.Ahn and C.Ruiz-Vargas, Nano Lett. **9** 5,1742-1746 (2009)

[35] G. Eda *et al.*, J.Phys. Chem. **113**,15768-15771 (2009)

[36] N.P.Guisinger *et al.* Nano Lett. **9** 4,1462-1466 (2009)

[37] M.Y. Han *et al.*, Phys. Rev. Lett **98**,206805 (2007)

[38] X. Li *et al.*,Science **319**,1229 (2008)

[39] I. Jung *et al*, Nano Letters **8** 12,4283-4287 (2008)

[40] J. Bai *et al.*, Nature Nanotechnology **5**,190 (2010)

[41] W. Choi *et al.*, Critical Reviews in Solid State and Materials Sciences **35**, 52 (2010)

[42] S. Wang *et al.*, Appl. Phys. Lett. **96**, 143109 (2010)

[43] J.A. Yan, L.Xian and M.Y.Chou, Phys.Rev.Lett. **103**,086802 (2009)

[44] D.W. Boukhalov and M.I. Katsnelson, J.Am.Chem.Soc. **130**,10697-10701 (2008)

[45] G.K. Ramesha, S. Sampath, J. Phys. Chemm. C **113** 19,7985 (2009)

[46] D.C. Elias *et al.*, Science **324**, 1530 (2009)

[47] C.C.Lee, T.A. Tran, L.Yong, F. Harun, C.C. Yong, Electronic Components and Technology Conference, (2003)